

Effect of Magnetic diffusion in the Chromosphere on the Solar Wind

MASATO MATSUOKA ¹, TAKERU K. SUZUKI ^{1,2}, TAKATO TOKUNO ^{1,3} AND KENSUKE KAKIUCHI ¹

¹*School of Arts & Sciences, The University of Tokyo, 3-8-1, Komaba, Meguro, Tokyo 153-8902, Japan*

²*Komaba Institute for Science, The University of Tokyo, 3-8-1 Komaba, Meguro, Tokyo 153-8902, Japan*

³*Department of Astronomy, The University of Tokyo, 7-3-1, Hongo, Bunkyo, Tokyo, 113-0033, Japan*

Submitted to ApJ

ABSTRACT

We investigate non-ideal magnetohydrodynamical (MHD) effects in the chromosphere on the solar wind by performing MHD simulations for Alfvén-wave driven winds with explicitly including Ohmic and ambipolar diffusion. We find that MHD waves are significantly damped in the chromosphere by ambipolar diffusion so that the Alfvénic Poynting flux that reaches the corona is substantially reduced. As a result, the coronal temperature and the mass loss rate of the solar wind are considerably reduced, compared with those obtained from an ideal MHD case, which is indicative of a great importance of the non-ideal MHD effects in the solar atmosphere. However, the temperature and the mass loss rate are recovered by a small increase in the convection-originated velocity perturbation at the photosphere because of the sensitive dependence of the ambipolar diffusion and reflection of Alfvén waves on the physical properties of the chromosphere. We also find that density perturbations in the corona are reduced by the ambipolar diffusion of Alfvén waves in the chromosphere because the nonlinear generation of compressible perturbations is suppressed.

Keywords: Stellar winds (1636) – Solar wind (1534) – Magnetohydrodynamical simulations (1966) – Alfvén waves (23)

1. INTRODUCTION

In the solar atmosphere, the ratio of the magnetic pressure to the gas pressure generally increases with elevating altitude (Gary 2001; Wiegmann et al. 2014). Magnetic fields play a vital role in the dynamics and thermodynamics of the plasma in upper layers of the atmosphere. Key outcomes of the magnetic dominance are heating the corona and driving the solar wind. One of the plausible mechanisms that heat and accelerate the plasma is magnetohydrodynamical (MHD) waves (Alfvén 1947; Osterbrock 1961; Uchida & Kaburaki 1974; Ofman & Davila 1995, see Van Doorselaere et al. (2020) for recent review) Convective motions beneath the photosphere excite various modes of waves. In particular, transverse (\approx Alfvénic) waves are considered to be reliable players in the upward transport of energy, unlike compressible waves, they can propagate a long

distance owing to the incompressible nature, avoiding shock dissipation as a consequence of steepening of wave front. Recently, transverse waves have been detected in the chromosphere (Okamoto & De Pontieu 2011; McIntosh et al. 2011; Jess et al. 2023; Yuan et al. 2023). and in the corona (Nakariakov et al. 1999; Tomczyk et al. 2007; Anfinogentov et al. 2015; Banerjee et al. 2021). Roles of Alfvénic waves in the heating and acceleration of the coronal plasma have also been investigated from a theoretical point of view (e.g., Alazraki & Courtourier 1971; Belcher 1971; Ionson 1978; Matsumoto 2018; Shoda et al. 2019).

A key is how the energy of excited Alfvén(ic) waves is exchanged for thermal and kinetic energies in the upper atmosphere. To this end, various mechanisms for wave dissipation have been proposed. Transverse waves are converted into compressible waves by nonlinear mode conversion (Hollweg 1982; Kudoh & Shibata 1999; Suzuki 2004; Suzuki & Inutsuka 2005; Matsumoto & Suzuki 2012; Sakaue & Shibata 2020) and paramet-

ric decay instability (Tenerani et al. 2017; Réville et al. 2018), and the compressible waves eventually dissipate through the formation of shock waves (Suzuki 2002). Alfvénic waves are also damped via turbulent cascade (Hollweg 1986; Matthaeus et al. 1999; Verdini & Velli 2007; Cranmer et al. 2007; Shoda et al. 2018a), phase mixing (Heyvaerts & Priest 1983; Sakurai & Granik 1984; McMurdo et al. 2023) and resonant absorption (Hollweg 1984; Okamoto et al. 2015; Antolin et al. 2015).

In the fully ionized corona and solar wind, magnetic diffusion is negligible, and then, the ideal MHD approximation can be safely adopted in these theoretical models and numerical simulations. However, the approximation is no longer valid in the photosphere and chromosphere where the temperature is too low to achieve sufficient ionization (Vernazza et al. 1981). As a result, non-ideal MHD effects play a substantial role in the evolution of magnetic fields there. In the denser photospheric region, the dominant process is the Ohmic diffusion that stems from the resistivity due to the collision between electrons and neutrals. In the less dense chromospheric region, the primary mechanism is the ambipolar diffusion induced by the drift motion between neutrals and magnetic fields coupled with charged particles (Leake et al. 2005; Khomenko et al. 2014; Soler et al. 2015; Martínez-Sykora et al. 2023)¹. In the latter case the frictional coupling between the neutral and charged components is not perfect owing to the low-density condition, and hence, the collision between neutrals and ions is the main agent for the magnetic dissipation (Mestel & Spitzer 1956; Brandenburg & Zweibel 1994; Zweibel 2015).

These non-ideal MHD effects promote the damping of MHD waves, leading to the heating of ambient gas (de Pontieu & Haerendel 1998; Khodachenko et al. 2004; Popescu Braileanu & Keppens 2021; Morton et al. 2023). A characteristic property is that higher-frequency waves are more significantly affected by magnetic diffusion; for example, ambipolar diffusion has a severe impact on Alfvénic waves with frequency higher than collisional frequency between ions and neutrals (Soler et al. 2013). Although these effects have been investigated in the photosphere and the chromosphere (e.g., Piddington 1956; Osterbrock 1961; Shelyag et al. 2016), it is poorly understood how those MHD waves that have undergone the non-ideal MHD diffusion in the low atmosphere travel to the corona and the solar wind. The objective of this pa-

per is to investigate the influence of the non-ideal MHD effect on the solar wind by performing numerical simulations from the photosphere to the solar wind with a self-consistent MHD model; We study how the physical properties of the corona and the solar wind are modified in the non-ideal MHD treatment, compared with those obtained under the ideal MHD approximation.

This paper is organized as follows. In section 2 we explain our simulation setup. In section 3 and 4 we show the main results and discuss related topics. We summarize the paper in section 5.

2. METHODS

We perform non-ideal MHD simulations in a one-dimensional (1D; hereafter) magnetic flux tube that covers from the photosphere at $r = R_\odot$ to $r = r_{\text{out}} = 40R_\odot$, where $R_\odot = 6.96 \times 10^6$ km is the solar radius. For that purpose, we extend an ideal MHD simulation model originally developed by Suzuki & Inutsuka (2005, 2006) for the solar wind from coronal holes.

2.1. Flux Tube Model

We adopt a super-radially open flux tube (Kopp & Holzer 1976; Suzuki et al. 2013) that does not change with time. Cross section A is given by $A = r^2 f$, where f is the filling factor modeled as

$$f(r) = \frac{e^{\frac{r-R_\odot-h}{\sigma}} + f_0 - (1-f_0)e^{-\frac{h}{\sigma}}}{e^{\frac{r-R_\odot-h}{\sigma}} + 1}. \quad (1)$$

We set $f_0 = f(R_\odot) = 1/1265$, $\sigma = (1/2)h$ and $h = 0.042 R_\odot$, where a small value of f_0 indicates that the solar surface is mostly occupied by closed magnetic loops. We determine $B_{r,0} = 1.48$ kG (see Section 2.4 for this specific value).

The radial component of magnetic field B_r is determined by the conservation of magnetic flux:

$$B_r(r) = B_{r,0} \frac{R_\odot^2 f_0}{r^2 f}. \quad (2)$$

2.2. Basic Equations

We solve non-ideal MHD equations including gravity, radiative cooling, thermal conduction, and phenomenological heating due to the turbulent cascade of Alfvénic waves. The followings are the equations for the conservation of mass, the conservation of radial and perpendicular momentums, the conservation of energy, and the evolution of magnetic fields, respectively:

$$\frac{\partial}{\partial t} \rho + \frac{1}{r^2 f} \frac{\partial}{\partial r} (\rho v_r r^2 f) = 0, \quad (3)$$

¹ We note that there is a regime where Hall diffusion is significant between the regions dominated by the Ohmic and ambipolar diffusion (Pandey et al. 2008), whereas we do not consider it in the current paper (see Section 2.3).

$$\begin{aligned} \frac{\partial}{\partial t}(\rho v_r) + \frac{1}{r^2 f} \frac{\partial}{\partial r} \left[\left(\rho v_r^2 + p + \frac{B_\perp^2}{8\pi} \right) r^2 f \right] \\ = \frac{1}{r^2 f} \left(\frac{\rho v_\perp^2}{2} + p \right) \frac{d}{dr} r^2 f - \rho \frac{GM_\odot}{r^2}, \end{aligned} \quad (4)$$

$$\begin{aligned} \frac{\partial}{\partial t}(\rho \mathbf{v}_\perp) + \frac{1}{r^3 f^{3/2}} \frac{\partial}{\partial r} \left[\left(\rho v_r \mathbf{v}_\perp - \frac{B_r \mathbf{B}_\perp}{4\pi} \right) r^3 f^{3/2} \right] \\ = \rho \mathbf{D}_{v_\perp}, \end{aligned} \quad (5)$$

$$\begin{aligned} \frac{\partial}{\partial t} e_{\text{tot}} + \frac{1}{r^2 f} \frac{\partial}{\partial r} \left[\left((e_{\text{tot}} + p_T) v_r - B_r \frac{\mathbf{B}_\perp \cdot \mathbf{v}_\perp}{4\pi} \right) r^2 f \right] \\ = \frac{1}{r^2 f} \frac{\partial}{\partial r} \left[\frac{\eta_{\text{tot}}}{4\pi} r \sqrt{f} \mathbf{B}_\perp \cdot \frac{\partial}{\partial r} (\mathbf{B}_\perp r \sqrt{f}) \right] \\ - \rho v_r \frac{GM}{r^2} + Q_{\text{rad}} + Q_{\text{cond}}, \end{aligned} \quad (6)$$

$$\begin{aligned} \frac{\partial}{\partial t} \mathbf{B}_\perp + \frac{1}{r \sqrt{f}} \frac{\partial}{\partial r} \left[(\mathbf{B}_\perp v_r - B_r \mathbf{v}_\perp) r \sqrt{f} \right] \\ = \sqrt{4\pi \rho} \mathbf{D}_{b_\perp} + \frac{1}{r \sqrt{f}} \frac{\partial}{\partial r} \left[\eta_{\text{tot}} \frac{\partial}{\partial r} \mathbf{B}_\perp r \sqrt{f} \right]. \end{aligned} \quad (7)$$

$\rho, v, p, e,$ and B are mass density, velocity, pressure, specific energy, and magnetic field, respectively. Subscripts r and \perp denote radial and perpendicular components. G is the gravitational constant and M_\odot is the solar mass. A vector \mathbf{a} in our coordinate system is expressed by these components as

$$\mathbf{a} = a_r \hat{\mathbf{e}}_r + a_{\perp 1} \hat{\mathbf{e}}_{\perp 1} + a_{\perp 2} \hat{\mathbf{e}}_{\perp 2}, \quad (8)$$

where $\hat{\mathbf{e}}$ is a unit vector.

$$e_{\text{tot}} = \rho e + \frac{1}{2} \rho v^2 + \frac{B_\perp^2}{8\pi} \quad (9)$$

and

$$p_T = p + \frac{B_\perp^2}{8\pi} \quad (10)$$

are total energy density and total pressure, respectively.

$$\eta_{\text{tot}} = \eta_O + \eta_{\text{AD}}. \quad (11)$$

is the sum of Ohmic and ambipolar diffusivities, which are described later in Section 2.3.

Q_{cond} represents conductive heating:

$$Q_{\text{cond}} = -\frac{1}{r^2 f} \frac{\partial}{\partial r} (F_c r^2 f), \quad (12)$$

where

$$F_c = \kappa_0 T^{5/2} \frac{\partial T}{\partial r} \quad (13)$$

is Spitzer-Härm-type conductive flux with $\kappa_0 = 10^6 \text{ g cm s}^{-3} \text{ K}^{-7/2}$ for electrons in fully ionized plasma under thermal equilibrium (Braginskii 1965; Matsumoto & Suzuki 2014). In weakly ionized gas with $T \lesssim 10^4 \text{ K}$, the expression of equation (13) should be replaced with the conductive flux carried by neutral particles (Parker 1953; Koyama & Inutsuka 2000). Although this correction is required below the transition region, the conduction term using the correct expression is largely dominated by other terms of equation (6) there. Coincidentally, this is also true even if equation (13) is used owing to the steep dependence of κ_0 on temperature. Hence, equation (13) is used in the entire simulation domain.

Q_{rad} represents radiative cooling, which is handled separately in optically thick and thin regimes (Suzuki 2018). In the low-temperature, $T < T_{\text{crt}} = 1.2 \times 10^4 \text{ K}$, region, we adopt an empirical cooling rate based on observations of the solar chromosphere introduced by Anderson & Athay (1989):

$$Q_{\text{rad}} = 4.5 \times 10^9 \times \rho \times \min \left(1, \frac{\rho}{\rho_{\text{crt}}} \right), \quad (14)$$

where $\rho_{\text{crt}} = 10^{-16} \text{ g cm}^{-3}$ is a critical density. Equation (14) gives $Q_{\text{rad}} \propto \rho$ in the high-density region to take into account the optically thick effect, which is in contrast to the normal dependence, $Q_{\text{rad}} \propto \rho^2$, in the low-density regime. In the high-temperature region, $T > T_{\text{crt}}$, we adopt an optically thin cooling for ionized plasma:

$$Q_{\text{rad}} = \Lambda n n_e. \quad (15)$$

where n is the ion number density and n_e is the electron number density. The cooling function, Λ , is adopted from the tabulated data by Sutherland & Dopita (1993). For numerical stability, we connect these two regimes smoothly across $T = T_{\text{crt}}$ by interpolating Q_{rad} 's obtained from equations (14) and (15).

Following Shoda et al. (2018a, see also Shimizu et al. (2022); Washinoue et al. (2022)) we consider the dissipation of Alfvénic waves via turbulence in a phenomenological way (Hossain et al. 1995; Cranmer et al. 2007). $D_{v_\perp i}$ and $D_{b_\perp i}$ in equations (5) and (7) denote turbulent dissipation coefficients of velocity and magnetic field amplitudes:

$$D_{v_\perp i} = -\frac{c_d}{4\lambda_{\perp i}} (|z_{\perp i}^+| |z_{\perp i}^-| + |z_{\perp i}^-| |z_{\perp i}^+|), \quad (16)$$

$$D_{b_\perp i} = -\frac{c_d}{4\lambda_{\perp i}} (|z_{\perp i}^+| |z_{\perp i}^-| - |z_{\perp i}^-| |z_{\perp i}^+|), \quad (17)$$

where

$$z_{\perp i}^{\pm} = v_{\perp i} \mp \frac{B_{\perp i}}{\sqrt{4\pi\rho}} \equiv v_{\perp i} \mp b_{\perp i}, \quad (18)$$

is Elsässer variables (Elsasser 1950). We set the nondimensional constant, $c_d = 0.1$, following van Ballegooijen & Asgari-Targhi (2017). λ is the correlation length that is dependent on r as

$$\lambda(r) = \lambda_0 \frac{r}{R_{\odot}} \sqrt{\frac{f(r)}{f_0}}. \quad (19)$$

We set $\lambda_0 = 10^3$ km. This value is based on the size of granule (Roudier & Muller 1986; Berger & Title 2001; Abramenko et al. 2012), whereas recent observation by the CoMP telescope reports a larger value of $\lambda_0 = 7.6 - 9.3 \times 10^3$ km (Sharma & Morton 2023).

2.3. Non-ideal MHD Effects

The Ohmic diffusion in the weakly ionized solar atmosphere is induced by the collision between electrons and neutrals. The corresponding diffusivity is derived (Spitzer 1962; Schmidt 1966; Blaes & Balbus 1994) as

$$\begin{aligned} \eta_0 &= \frac{c^2 m_e \nu_{en}}{4\pi e^2 n_e} \\ &\simeq 2.3 \times 10^2 \frac{\max((1-x_e), 0)}{x_e} \sqrt{\frac{T}{\text{K}}} \text{ cm}^2 \text{ s}^{-1}, \end{aligned} \quad (20)$$

where c is the speed of light, e_e is the elementary charge, and m_e is the electron mass. Subscripts i, e and n stand for ion, electron, and neutral species, respectively. $\nu_{en} = n_n \overline{\sigma_{en} v_{en}}$ is the collision frequency between electrons and neutrals, where σ_{en} and v_{en} are respectively the cross section and the relative velocity between electrons and neutrals; the overline means the average over the velocity space, and $\overline{\sigma_{en} v_{en}} = 8.3 \times 10^{-10} T/\text{K cm}^3 \text{ s}^{-1}$ (Draine et al. 1983). x_e is the ionization degree, which is modeled below².

The ambipolar diffusivity can be approximately calculated (Khomenko & Collados 2012) as

$$\begin{aligned} \eta_{\text{AD}} &= \frac{B^2 (\rho_n / \rho)^2}{4\pi \chi \rho_i \rho_n} \\ &\simeq 2.1 \times 10^{-16} \frac{(B/G)^2 \max((1-x_e), 0)^2}{[\rho / (\text{g cm}^{-3})]^2 x_e} \text{ cm}^2 \text{ s}^{-1}, \end{aligned} \quad (21)$$

² The max function in equations (20) and (21) is used to avoid negative $1 - x_e$ because x_e slightly exceeds 1 in fully ionized gas for the definition of equation (22). The physical origin of the $(1 - x_e)$ component is neutral number density (Khomenko & Collados 2012), which also $\rightarrow 0$ for fully ionized conditions, then, this approximated treatment can be justified.

where $\chi = \overline{\sigma_{in} v_{in}} / (m_i + m_n)$ with $\overline{\sigma_{in} v_{in}} = 1.9 \times 10^{-9} \text{ cm}^3 \text{ s}^{-1}$ (Draine et al. 1983).

We calculate the ionization degree, following Yasuda et al. (2019), see also Hartmann & Avrett (1984); Harper et al. (2009):

$$\begin{aligned} x_e = \frac{n_e}{n_{\text{H}}} &= \frac{n_p}{n_{\text{H}}} + \frac{n_{\text{He}^+}}{n_{\text{H}}} + 2 \frac{n_{\text{He}^{++}}}{n_{\text{H}}} \\ &+ \sum_{j=1}^J A_j \left(\frac{R_{c1}^j}{R_{1c}^j} + 1 \right)^{-1}. \end{aligned} \quad (22)$$

where $n_{\text{H}}, n_p, n_{\text{He}^+}$, and $n_{\text{He}^{++}}$ are number densities of hydrogen nuclei, protons, first-ionized helium ions, and second-ionized helium ions, respectively. In addition to H and He, we take into account C, O, Na, Mg, Al, Si, S, K, Ca, Cr, and Fe. A_j denotes abundance of j -th element. We adopt the standard solar abundances by Asplund et al. (2009). The number density ratios on the right-hand side are derived from the Saha equation; e.g., the ionization of hydrogen is given by

$$\frac{n_p}{n_{\text{H}}} = \frac{1}{n_{\text{H}}} \left(\frac{2\pi m_e k_{\text{B}} T}{h^2} \right)^{3/2} \exp\left(-\frac{I_{\text{H}}}{k_{\text{B}} T}\right), \quad (23)$$

where k_{B} and I_{H} are the Boltzmann constant and the ionization energy of hydrogen, respectively. R_{c1} and R_{1c} in equation (22) are the photoionization and radiative recombination rates, respectively; the ratio is calculated as

$$\begin{aligned} \frac{R_{1c}^j}{R_{c1}^j} &= \frac{1}{n_e T} \left(\frac{2\pi m_e k_{\text{B}} T}{h^2} \right)^{3/2} \left[W T_{\text{eff}} e^{-h\nu_{1,0}/(k_{\text{B}} T_{\text{eff}})} \right. \\ &\left. + W_{\text{gal}} T_{\text{gal}} e^{-h\nu_{1,0}/(k_{\text{B}} T_{\text{gal}})} \right], \end{aligned} \quad (24)$$

where $\nu_{1,0}$ is the frequency of the photoionization edge. In the first term of equation (24) we approximated the radiation field of the sun by black body radiation with the effective temperature, $T_{\text{eff}} = 5780$ K. Geometric dilution factor W is defined as

$$W = \frac{1}{2} \left[1 - \sqrt{1 - \left(\frac{R_{\odot}}{r} \right)^2} \right]. \quad (25)$$

We are also considering galactic ionization in the second term of equation (24), which comes from the interstellar radiation field. Following Mathis et al. (1983), we set $T_{\text{gal}} = 7500$ K and $W_{\text{gal}} = 10^{-14}$.

It should be noted that we ignore the Hall term, which generates one tangential component of magnetic field from the other tangential component and the part of the ambipolar diffusion terms that requires the nonlinear coupling between the two tangential components. Their contributions are supposed to be smaller than the currently included terms. For a detailed explanation, see Appendix A.

2.4. Boundary Condition

At the inner boundary, $r = R_\odot$, we set $T_{\text{eff}} = 5780$ K. We adopt $\rho_0 = 2.5 \times 10^{-7}$ g cm $^{-3}$ from the ATLAS model atmosphere (Kurucz 1979; Castelli & Kurucz 2003). At the inner boundary, we assume that gas pressure and magnetic pressure are in equilibrium (Suzuki et al. 2013):

$$\frac{8\pi p_0}{B_{r,0}^2} = 1. \quad (26)$$

Here, the gas pressure is related with ρ_0 and T_{eff} through the equation of state:

$$p_0 = (\rho_0/\mu_0 m_u) k_B T_{\text{eff}}, \quad (27)$$

where m_u is the atomic mass unit and $\mu_0 = 1.2$ is the mean molecular weight at the photosphere, respectively. From equations (26) and (27), we determine $B_{r,0} = 1.48$ kG (Section 2.1).

We set velocity perturbation in a wide frequency band at the inner boundary,

$$\langle \delta v_0^2 \rangle = \int_{\omega_{\min}}^{\omega_{\max}} P(\omega) d\omega, \quad (28)$$

from $1/\omega_{\min} = 30$ min to $1/\omega_{\max} = 0.3$ min, where $P(\omega)$ is assumed to be proportional to ω^{-1} .

Vertical and horizontal velocities at the photosphere have been observed by Doppler technique (e.g., Oba et al. 2017) and feature tracking method (e.g., November & Simon 1988). The obtained results exhibit a wide range from 0.37 km s $^{-1}$ to 2.4 km s $^{-1}$ (Title et al. 1989; Oba et al. 2020). In this study, as a fiducial value, we adopt $\langle \delta v_0 \rangle = 1.25$ km s $^{-1}$ for both transverse and longitudinal fluctuations, which is consistent with observational values taken by Berger et al. (1998); Matsumoto & Kitai (2010); Chitta et al. (2012).

The outer boundary of the simulation region is set at $r = r_{\text{out}} = 40R_\odot$. Above $r = r_{\text{out}}$, the cell size, Δr , is enlarged and the domain covers up to $r \approx 80R_\odot$ where we prescribe the outgoing boundary condition for mass and waves (Suzuki & Inutsuka 2005, 2006).

2.5. Initial Condition

We start our simulations from the hydrostatic density structure with $T = T_{\text{eff}}$ in the low atmosphere where $\rho > \rho_{\text{turn}} = 2.5 \times 10^{-13}$ g cm $^{-3}$. In the high-altitude region where $\rho < \rho_{\text{turn}}$, we set up higher density than the hydrostatic value to avoid unphysically high Alfvén speed, which severely limits the time step of the simulations. The initial density profile is shown in Figure 1. Although the gas initially infalls from the outer over-dense region, it is eventually blown outward by denser outflows from the lower region. We confirm that the final steady-state wind profile is not affected by a choice

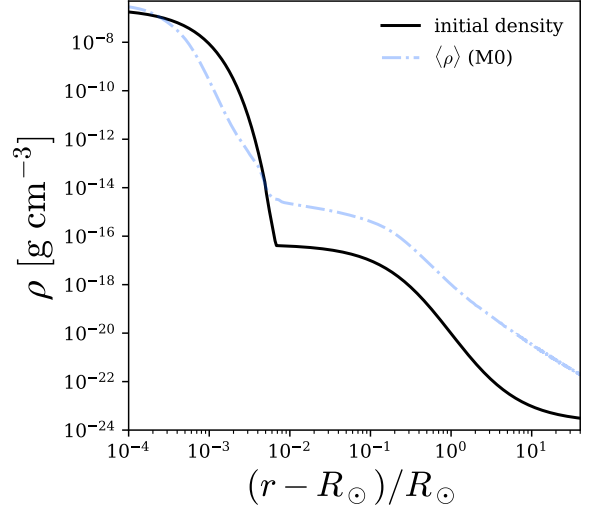


Figure 1. Initial density profile (black solid) and time-averaged radial density profile of ideal MHD case, M0 (light blue dash-dotted; see Section 3.2).

of ρ_{turn} provided that the sufficiently small ρ_{turn} is employed.

2.6. Simulation Cases

The main purpose of this paper is to investigate roles of magnetic diffusion in the heating and acceleration of coronal plasma. To this end, firstly we perform four cases, M0 – M3, presented in Table 1 for the fixed $\langle \delta v_0 \rangle$ in Section 3.1, 3.2, 3.3, and 3.4; in each case resistivity and ambipolar diffusion are respectively switched on and off. In addition, we also examine the dependence on the input velocity perturbation, $\langle \delta v_0 \rangle$, in Section 3.5.

We conduct the simulations until $t = 6t_{\text{sim}}$, where $t_{\text{sim}} = R_\odot/c_{s,0}$ is time in simulation units with the sound speed, $c_{s,0}$, at the photosphere. We verify that the simulation time is sufficiently long because after $t \gtrsim 3t_{\text{sim}}$ quasi time-steady profiles are achieved in the atmosphere and the wind region. We note that the simulation time, $6t_{\text{sim}}$, corresponds to 10 times the Alfvén crossing time, $40R_\odot/\langle v_A \rangle$, over the simulation domain, where $\langle v_A \rangle \approx 477$ km s $^{-1}$ is the average Alfvén velocity from the corona to the solar wind.

In Sections 3 and 4 we compare various physical quantities averaged over time. We express $\langle A \rangle$ for the average of a quantity, A , from $t = 3t_{\text{sim}}$ to $6t_{\text{sim}}$.

2.7. Energetics Formulation

Under the quasi-steady state, energy balance (equation 6) is reduced to

$$\begin{aligned} \frac{d}{dr}(L_A + L_K + L_E - L_G - L_C - L_D + L_R) \\ \equiv \frac{d}{dr}L_{\text{tot}} \approx 0, \end{aligned} \quad (29)$$

where total energy luminosity L_{tot} is composed of Alfvén luminosity L_A , kinetic luminosity L_K , enthalpy luminosity L_E , gravitational luminosity L_G , conductive luminosity L_C , diffusive luminosity L_D , and radiative loss L_R (Suzuki et al. 2013; Shimizu et al. 2022). They are expressed as follows:

$$L_A = \left[v_r \left(\rho \frac{v_\perp^2}{2} + \frac{B_\perp^2}{4\pi} \right) - B_r \frac{v_\perp B_\perp}{4\pi} \right] 4\pi r^2 f, \quad (30)$$

$$L_K = \frac{1}{2} \rho v_r^3 4\pi r^2 f, \quad (31)$$

$$L_E = \frac{\gamma}{\gamma - 1} p v_r 4\pi r^2 f, \quad (32)$$

$$L_G = \rho v_r \frac{GM_\odot}{r} 4\pi r^2 f = \dot{M} \frac{GM_\odot}{r}, \quad (33)$$

$$L_C = \kappa_0 T^{5/2} \frac{\partial T}{\partial r} 4\pi r^2 f, \quad (34)$$

$$L_D = \left[\frac{\eta_{\text{tot}}}{4\pi r \sqrt{f}} \mathbf{B}_\perp \cdot \frac{\partial}{\partial r} (\mathbf{B}_\perp r \sqrt{f}) \right] 4\pi r^2 f, \quad (35)$$

and

$$L_R = - \int_r^{r_{\text{out}}} 4\pi r^2 f Q_{\text{rad}}, \quad (36)$$

where the factor, $r^2 f$, is included to compensate the adiabatic expansion effect and

$$\dot{M} = 4\pi r^2 f \rho v_r. \quad (37)$$

is the mass loss rate by winds. Radiation loss, L_R , in equation (36) at r is evaluated by the integration from r to r_{out} .

The sum of L_A and L_D is originally from the radial component of Poynting flux:

$$\begin{aligned} \frac{L_A + L_D}{4\pi r^2 f} &= \frac{1}{4\pi} (\mathbf{E} \times \mathbf{B})_r \\ &= \frac{1}{4\pi c} [(-\mathbf{v} \times \mathbf{B} + \eta_{\text{tot}} \nabla \times \mathbf{B}) \times \mathbf{B}]_r. \end{aligned} \quad (38)$$

The first term, which indicates the Poynting flux carried by Alfvénic waves, can be separated into the outgoing component,

$$L_{A,+} = \rho (z_\perp^+)^2 (v_r + v_A) \pi r^2 f, \quad (39)$$

and the incoming component,

$$L_{A,-} = \rho (z_\perp^-)^2 (v_r - v_A) \pi r^2 f. \quad (40)$$

We note that $L_A = L_{A,+} + L_{A,-}$ is satisfied; L_A indicates the net outgoing luminosity. The second term of equation (38) is the "diffusive" (or "dissipative") Poynting flux arising from magnetic diffusion.

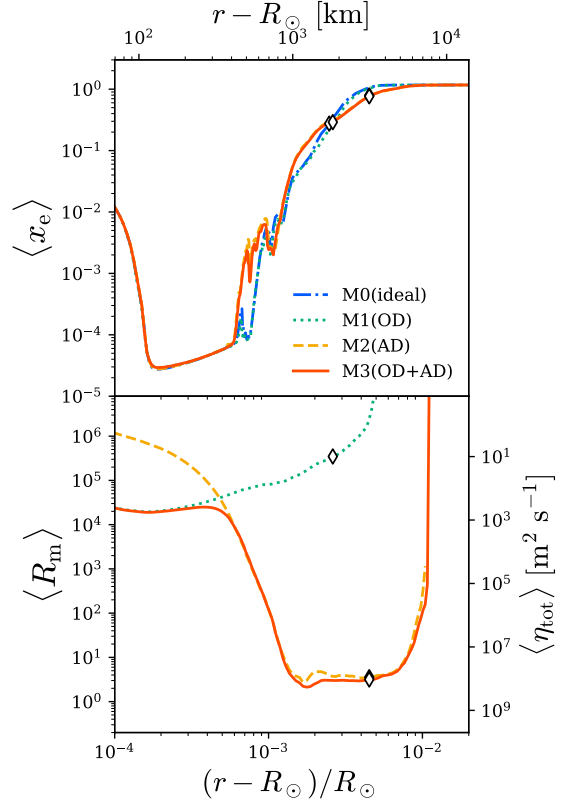


Figure 2. Time-averaged ionization fraction x_e and magnetic Reynolds number R_m of cases with M0 (blue dash-dotted), M1 (green dotted), M2 (orange dashed), and M3 (red solid). "OD" and "AD" stand for Ohmic and ambipolar diffusion, respectively. These panels share horizontal axis; top and bottom axes are in units of km and R_\odot , respectively. Diamonds represent the location where $T = 2 \times 10^4$ K.

3. RESULTS

3.1. Magnetic Diffusivity

Figure 2 shows the time-averaged radial profile of ionization fraction x_e (top) and magnetic Reynolds number R_m (bottom), defined below, in the low atmospheric region. Diamond markers correspond to the location where the time-averaged temperature reaches 20000 K, which corresponds to the top of the chromosphere and the bottom of the transition region. Below this point the plasma is partially ionized and non-ideal MHD effects are non-negligible. In $100 \text{ km} \lesssim r \lesssim 400 \text{ km}$, the ionization degree is kept small, $x_e < 10^{-5}$, because the temperature there is 4000 – 5000 K (see Section 3.2 and top panel of Figure 3) so that hydrogen is not ionized; in this region elements with low first ionization potential, such as Na and K, are the only ionization sources. Above $r - R_\odot \gtrsim 400 \text{ km}$ ($\approx 6 \times 10^{-4} R_\odot$), x_e increases with height as the temperature gradually increases in

the chromosphere. Fully ionized condition is satisfied in and above the transition region.

We defined magnetic Reynolds number,

$$R_m = \frac{VL}{\eta_O + \eta_{AD}}, \quad (41)$$

where $V = 10 \text{ km s}^{-1}$ and $L = 100 \text{ km}$ are employed for typical velocity and spatial scales, respectively, following [Khomenko & Collados \(2012\)](#); these values roughly correspond to the sound velocity and the pressure scale height in the chromosphere. We note that the magnetic diffusivity is exactly inversely proportional to R_m for constant V and L .

In the bottom panel of Figure 2, we focus on R_m of M3, which includes both Ohmic and ambipolar diffusion, as the comparison of the three cases, M1-M3, indicates that the total diffusivities, $\eta_O + \eta_{AD}$, in M3 is almost equal to the sum of η_O in M1 and η_{AD} in M2, which respectively include either Ohmic or ambipolar diffusion. In the photospheric region, $r \lesssim 500 \text{ km}$, where the density is high, the Ohmic diffusion dominates the ambipolar diffusion. However, R_m exceeds 10^4 , which means that the magnetic diffusion is not substantial there. In $r \gtrsim 500 \text{ km}$, the ambipolar diffusion dominates and R_m decreases with height as $\eta_{AD} (\propto x_e^{-1} \rho^{-2})$ increases, because the increase in x_e (top panel of Figure 2) is overwhelmed by the rapid decrease in the density (middle panel of Figure 3). R_m reaches the minimum value $R_m = 1 - 10$ at $r \approx 10^3 \text{ km}$ and stays $R_m < 10$ in the middle and upper chromosphere, $r \lesssim 5000 \text{ km}$ ($\approx 1.007 R_\odot$). In this region, the ambipolar diffusion significantly affects the propagation and dissipation of MHD waves, which will be discussed in the rest of the paper. At the transition region, R_m jumps up as the plasma becomes fully ionized so that the ideal-MHD condition is fulfilled in and above the corona. These properties of R_m from the photosphere to the corona is consistent with what are obtained in previous works ([Khomenko & Collados 2012](#); [Martínez-Sykora et al. 2012](#)).

3.2. Wind Structures

Figure 3 shows the time-averaged radial profiles of temperature (top), density (middle), and radial velocity (bottom). Substantial differences from the ideal MHD case (M0) are obtained when ambipolar diffusion is included (M2 and M3). The effect of the Ohmic diffusion (M1) is almost negligible except for a small difference in the radial velocity in the outer region, $r > 10 R_\odot$.

The cases with ambipolar diffusion give slightly higher temperature in the chromosphere (top panel of Figure 3) because of ambipolar diffusive heating; the transverse waves excited from the photosphere are partially

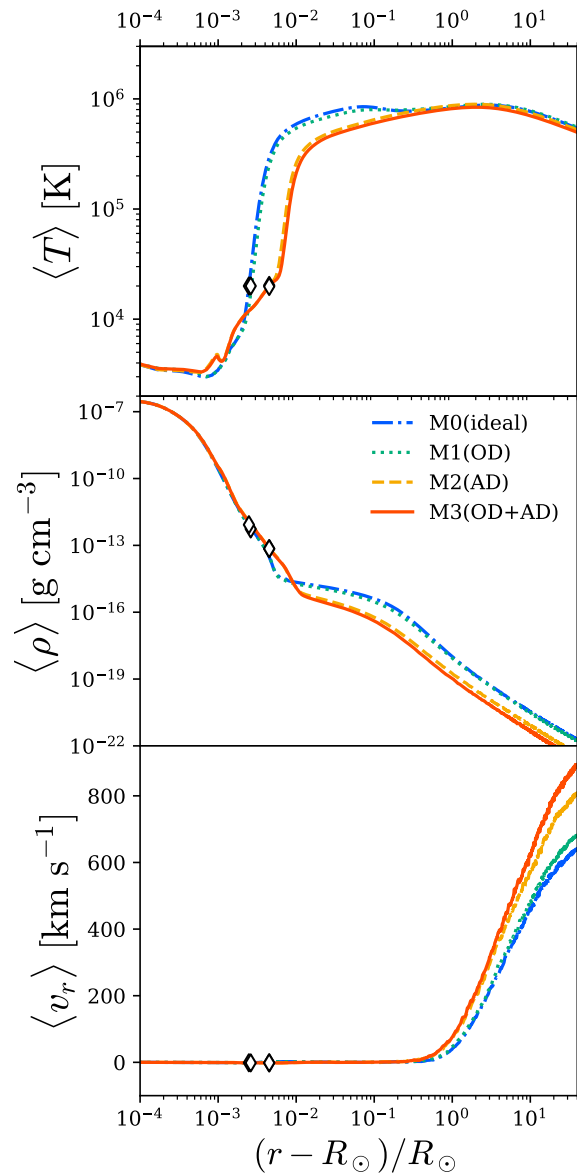


Figure 3. Time-averaged wind structures of the four cases, M0-M3. The line types and colors are the same as in Figure 2. From top to bottom, density, temperature, and radial velocities are presented. Diamonds represent the location where $T = 2 \times 10^4 \text{ K}$.

damped by ambipolar diffusion in the chromosphere, which transfers the wave energy to heat ([Khomenko & Collados 2012](#)). This works as an additional heating source to the dissipation of shock waves ([Arber et al. 2016](#)), which is the dominant source in the chromospheric heating in our simulations.

The effective dissipation in the chromosphere reduces the Poynting flux carried by the Alfvénic waves reaching the corona. As a result, the coronal heating is suppressed in the cases with ambipolar diffusion, giving

lower temperature in the low coronal region of M2 and M3. The lower temperature there reduces the downward thermal conductive flux. Therefore, the evaporation of denser chromospheric gas to the corona is suppressed, and consequently, the transition region that divides the chromosphere and the corona is located at a higher altitude (diamonds in Figure 3), leading to the lower density at the coronal base. Accordingly, the density in the corona and the solar wind is also lower in these cases (M2 and M3) than that obtained in the cases without ambipolar diffusion (M0 and M1) (middle panel of Figure 3). The mass loss rate of the former cases is also smaller as shown in Table 1 (see also Section 3.3).

In the coronal region above $r - R_\odot \gtrsim 0.5R_\odot$, the temperatures of the four cases converge. While in the cases with ambipolar diffusion, the Poynting flux reaching the corona is smaller (Section 3.3), at the same time the density is also lower. Hence, sufficient heating rate per mass is achieved to reach $T \gtrsim 10^6$ K even in these cases.

The bottom panel of Figure 3 indicates that the wind speed of all the cases reaches several hundred km s^{-1} near the outer boundary, which is an order of the escape velocity $\approx 620 \text{ km s}^{-1}$ from the Sun. A closer inspection shows the anti-correlation between the final wind velocity and the density; it is easier to accelerate less dense wind to higher velocity.

We would like to emphasize that, even though the non-ideal MHD effects are only important below the transition region, they make a considerable impact on the corona and the wind as shown in Figure 3. We examine detailed properties of the propagation and dissipation of waves in the presence of magnetic diffusion below.

3.3. Energetics

Figure 4 compares Alfvénic luminosities of M0 (left), M1 (middle), and M3 (right). In each panel, $L_{A,+}$, $L_{A,-}$ and L_A (equations 39, 40 and 30) are plotted. The outgoing Alfvénic luminosity at the solar surface,

$$L_{A,0} = - \left(B_r \frac{\langle v_\perp B_\perp \rangle}{4\pi} \right)_{r=R_\odot} 4\pi R_\odot^2 f_0, \quad (42)$$

in Table 1 is evaluated from the numerical data at 6 km (= average of four grid points from the inner boundary) above the inner boundary to avoid the effect of the boundary condition. M0–M3 yield $L_{A,+0} \approx (9.0 - 9.1) \times 10^{28} \text{ erg s}^{-1}$ with the difference among the four cases being less than 1%. We note that these values are smaller than the value estimated from $\rho \langle \delta v_0^2 \rangle v_{A,0} 4\pi R_\odot^2 f_0 \approx 1.5 \times 10^{29} \text{ erg s}^{-1}$. This is because the only velocity perturbation is input from the photosphere without magnetic fluctuation; both outgoing and incoming Poynting fluxes are injected, giving the smaller $L_{A,+0}$ than the simple estimate.

In the presented three cases, the incoming component, $L_{A,-}$, (green dotted in Figure 4) follows the outgoing component, $L_{A,+}$, (blue dashed) with a slightly smaller level. This indicates that a large fraction of the injected outgoing component is reflected back downward (Moore et al. 1991; Suzuki & Inutsuka 2006). The comparison between $L_{A,+0} = 9.1 \times 10^{28} \text{ erg s}^{-1}$ of M0 in Table 1 and the net outgoing luminosity, $L_A = 1.9 \times 10^{28} \text{ erg s}^{-1}$, of the same case in the photosphere (red solid line in the left panel of Figure 4) illustrates that about more than 90% of the input Alfvénic Poynting flux is reflected back to the photosphere. The reflection fractions of the dissipative cases, M1 and M3, are a little smaller but are still large, $\approx 87\%$ and, $\approx 83\%$, respectively.

The radial distribution of the Alfvénic luminosities in M1 is different from that of M0 only in the photosphere and the low chromosphere, $r - R_\odot < 10^{-3}R_\odot$, where the Ohmic resistivity is non-negligible. The incoming mode is slightly more suppressed than the outgoing one there to give the larger net outgoing luminosity, L_A , (red solid line in the middle panel of Figure 4) near the inner boundary. On the other hand, L_A and $L_{A,\pm}$ of M3 show a rapid drop at $r - R_\odot \approx 10^{-3}R_\odot$ in the chromospheric region owing to the efficient ambipolar diffusion. As a result, the Alfvénic luminosity that reaches the transition region, $L_{A,tc}$, of M3 is about $\approx 1/3$ of that of M0 (Table 1), where "tc" stands for the top of the chromosphere at $T = 2 \times 10^4$ K.

In order to examine the dissipation of Alfvénic waves in the chromosphere, we show the diffusive Poynting luminosity, L_D , (red) in addition to L_A (blue), below the low corona in Figure 5. We note that L_D is multiplied by a factor of 1000 to fit within the vertical range of Figure 5. The peaks of L_D at $r - R_\odot = 2 \times 10^{-4}R_\odot$ in M1 and M3 and at $r - R_\odot = 1.5 \times 10^{-3}R_\odot$ in M2 and M3 are due to Ohmic and ambipolar diffusion, respectively. Around these peaks, L_A of the corresponding cases rapidly decreases, as L_A is converted to L_D there; the magnetic diffusion plays an essential role in the dissipation of the Alfvénic waves. However, we should note that the value of L_D is much smaller than that of L_A . This is because the excited L_D , which consists of the diffusive part of electric field (equation 38), is almost instantly converted to heat and eventually lost by radiative cooling.

The Alfvénic Poynting luminosity that survives at the transition region basically determines the available energy to heat the corona and drive the wind. The key is that larger $L_{A,tc}$ results in larger density at the coronal base (middle panel of Figure 3) because larger heating by the dissipation of Alfvénic waves in the corona induces more efficient chromospheric evaporation (Section 3.2). Consequently, the kinetic energy luminosity,

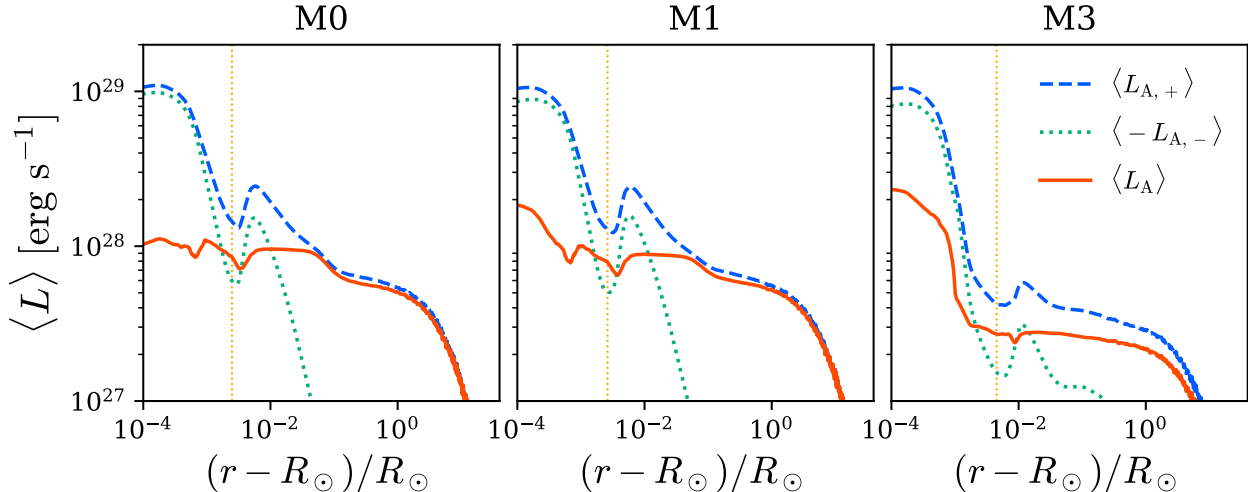


Figure 4. Time averaged radial profile of $L_{A,+}$ (blue dashed), $L_{A,-}$ (green dotted) and L_A red solid, for cases of M0 (left), M1 (middle), and M3 (right). Vertical dotted orange line represents where $T = 2 \times 10^4$ K.

Table 1. Input parameters and time-averaged output values.

model	non-ideal MHD effects	$\langle \delta v_0 \rangle$ (km s $^{-1}$)	$L_{A,+0}$	$L_{A,tc}$	$L_{A,out}$	$L_{K,out}$	$L_{R,tc}$	$L_{G,tc}$	\dot{M} (M_{\odot} yr $^{-1}$)
M0	$\eta_{\odot} = \eta_{AD} = 0$	1.25	91.1	8.49	0.19	2.77	3.41	2.45	2.04×10^{-14}
M1	$\eta_{\odot} \neq 0, \eta_{AD} = 0$	1.25	90.7	7.79	0.21	2.85	2.51	2.21	1.83×10^{-14}
M2	$\eta_{\odot} = 0, \eta_{AD} \neq 0$	1.25	90.6	3.66	0.13	1.27	0.79	0.70	5.82×10^{-15}
M3	$\eta_{\odot} \neq 0, \eta_{AD} \neq 0$	1.25	90.4	2.70	0.11	0.94	0.60	0.42	3.52×10^{-15}
M3-149	$\eta_{\odot} \neq 0, \eta_{AD} \neq 0$	1.49	128	8.39	0.20	2.95	2.05	2.41	2.01×10^{-14}
M3-170	$\eta_{\odot} \neq 0, \eta_{AD} \neq 0$	1.70	166	13.0	0.19	3.65	5.40	4.30	3.57×10^{-14}

Note. The luminosity of each component is explained in Section 2.7. The subscript "tc" or "out" indicates that the corresponding L is evaluated at $r = r_{tc}$ or $r = r_{out} (= 40R_{\odot})$. Mass loss rate \dot{M} is evaluated at $r = r_{out}$.

$L_{K,out}$ ($\propto \rho v_r^3$; equation 31), and the mass loss rate, \dot{M} ($\propto \rho v_r$; equation 37), are mostly correlated with $L_{A,tc}$ as shown in Table 1 whereas the detailed dependences of $L_{K,out}$ and \dot{M} on $L_{A,tc}$ are a little different because the density and velocity in the wind region are anti-correlated (bottom and middle panels of Figure 3); for example, $L_{K,out}$ of M1 is slightly larger than $L_{K,out}$ of M0 in spite of the smaller $L_{A,tc}$ and \dot{M} as the larger v_r compensates the smaller ρ in $L_{K,out}$.

The density at the coronal base also controls the energy loss from the corona. We are presenting radiative and gravitational losses evaluated at $r = r_{tc}$ in Table 1, where the integration for L_R is taken from $r = r_{tc}$ to r_{out} . We note that $L_{G,tc}$ is exactly proportional to the density at $r = r_{tc}$ (see equation 33) and that L_R practically includes the conductive loss, L_c , because the downward conductive flux from the corona to the chromosphere radiates away (Rosner et al. 1978; Washinoue & Suzuki 2023). Since the radiative cooling is proportional to ρ^2 in the optically thin corona (equation 15),

higher coronal density enhances $L_{R,tc}$. Therefore, M0 gives the largest $L_{R,tc}$ among the four cases, M0–M3.

The comparison between M0 and M3 indicates that the non-ideal MHD effects reduce the mass loss rate \dot{M} by a factor of 6. \dot{M} of the ideal MHD case, M0, is calibrated to explain the observational value $\approx 2 \times 10^{-14} M_{\odot}$ yr $^{-1}$ (Withbroe 1988; Wood et al. 2005, 2021), indicating that the cases with ambipolar diffusion (M2 and M3) cannot reproduce the average \dot{M} of the current solar wind (Table 1). However, we would like to note that there are still a number of freedoms in our setup; we particularly focus on the effect of the velocity perturbation at the photosphere on the global properties of the wind in Section 3.5.

3.4. Dissipation and Reflection of Transverse Waves

Figure 6 compares the time-averaged and root-mean-squared (rms) amplitudes of magnetic, $\langle b_{\perp} \rangle$ ($\equiv \sqrt{\langle B_{\perp}^2 \rangle} / \sqrt{4\pi \langle \rho \rangle}$), (blue) and velocity, $\langle v_{\perp} \rangle$ ($= \sqrt{\langle v_{\perp}^2 \rangle}$), (red) amplitudes for M0 (dotted), M3 (solid), and M3-

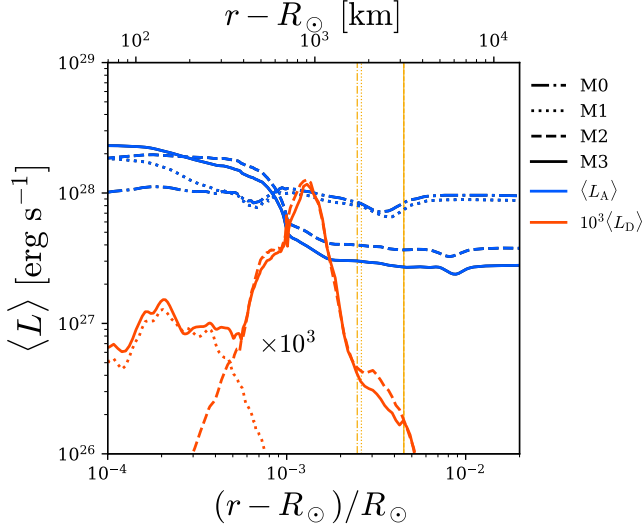


Figure 5. Time-averaged L_A (blue) and L_D (red) of M0–M3 in the chromosphere, where L_D is multiplied by 10^3 to fit within the displayed range. The line types are the same as in Figure 2. Orange vertical lines represent the location of the top of the chromosphere at $T = 2 \times 10^4$ K.

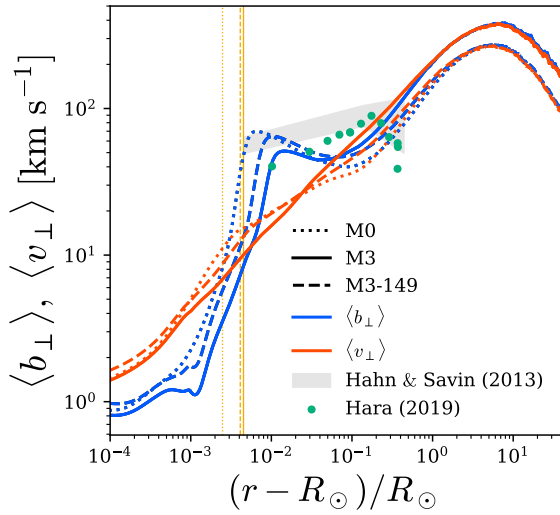


Figure 6. Time-averaged rms magnetic (blue) and velocity (red) amplitudes of transverse fluctuations for M0 (dotted), M3 (solid), and M3-149 (dashed). The altitude where $T = 2 \times 10^4$ K is plotted by orange vertical lines. The shaded region and green circles are observed nonthermal broadening by Hahn & Savin (2013) and Hara (2019), respectively.

149 (dashed; see Section 4.1). These cases show $\langle v_{\perp} \rangle > \langle b_{\perp} \rangle$ in the chromosphere; particularly in the cases with magnetic diffusion ($\langle b_{\perp} \rangle$) is decreased at $r - R_{\odot} \approx 10^{-3} R_{\odot}$ in the upper chromosphere owing to ambipolar diffusion (equation 7). However, $\langle b_{\perp} \rangle$ rapidly increases in the transition region, leading to $\langle b_{\perp} \rangle > \langle v_{\perp} \rangle$ in the low

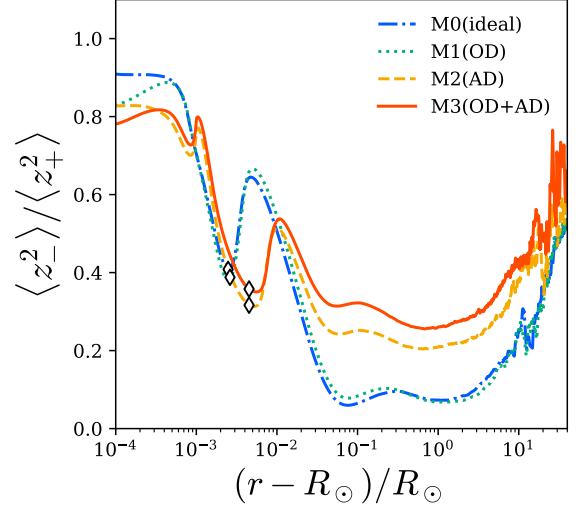


Figure 7. Time-averaged radial profile of the Elsässer ratio ($\mathcal{R}_E \equiv \langle z_{-}^2 \rangle / \langle z_{+}^2 \rangle$), where the line styles are the same as in Figure 2. Diamond markers represent the location of the top of the chromosphere at $T = 2 \times 10^4$ K.

corona. This indicates that the magnetic fluctuation behaves in a sense to conserve $B_{\perp} (= b_{\perp} \sqrt{4\pi\rho})$ across the transition region with a huge density gap (Verdini et al. 2012, see also Grappin et al. (2008)).

The inequality between $\langle v_{\perp} \rangle$ and $\langle b_{\perp} \rangle$ in the low atmosphere reflects the fact that the transverse perturbations are not in a simple Alfvénic state but the injected outgoing Alfvén waves are substantially reflected because of the variation in the Alfvén speed (Hollweg 1984; An et al. 1990; Suzuki & Inutsuka 2006; Shoda & Yokoyama 2016). The wave reflection is the primary reason why the only tiny fraction of the input energy, $L_{A,+0}$, can contribute to the kinetic energy of the solar wind (Table 1 and Section 3.2). To inspect the detailed properties of the reflection, Figure 7 compares Elsässer ratio, $\mathcal{R}_E \equiv \langle z_{-}^2 \rangle / \langle z_{+}^2 \rangle$ of M0 (dash-dotted), M1 (dotted), M2 (dashed), and M3 (solid). From the photosphere to the low chromospheric region, $r - R_{\odot} \lesssim 10^{-3} R_{\odot}$, \mathcal{R}_E is smaller in diffusive cases. This is because reflected waves, which have traveled a longer distance at a given r than the outgoing waves coming directly from the photosphere, are more severely damped by non-ideal MHD effects. The location of the local peak in \mathcal{R}_E around $10^{-2} R_{\odot}$ coincides with the transition region where the Alfvén velocity most drastically changes owing to the drop in the density. The peak value of \mathcal{R}_E is smaller in M2 and M3 with ambipolar diffusion because the density drop at the transition is smaller at the transition region (middle panel of Figure 3), which is due to the smaller temperature jump (top panel) as a result of the suppressed chromospheric evaporation (Section 3.2).

The lower coronal temperature due to the suppressed chromospheric evaporation also leads to the faster decrease of the coronal density as the pressure scale height is smaller. As a result, more efficient reflection takes place in the corona and wind regions of M2 and M3 to give larger \mathcal{R}_E . In other words, the non-ideal MHD effects in the chromosphere indirectly reduce the energy transport by Alfvénic waves in the corona through the promoted wave reflection. However, even in M2 and M3, \mathcal{R}_E is still not large $\lesssim 0.4$ in $r - R_\odot \lesssim 10R_\odot$, namely the Alfvénic Poynting flux is dominated by the outgoing component, being in $\langle v_\perp \rangle \approx \langle b_\perp \rangle$ as shown in Figure 6.

3.5. Dependence on $\langle \delta v_0 \rangle$

So far we have fixed the velocity perturbation at the photosphere to $\langle \delta v_0 \rangle = 1.25 \text{ km s}^{-1}$. While this is a typical value as discussed in Section 2.4, observational data exhibit a reasonably large range. For example, Oba et al. (2020) reviewed that horizontal convective velocities by various observations are ranging from 0.37 km s^{-1} to 2.4 km s^{-1} . In this subsection, we investigate the dependence of the structure of the atmosphere and wind on $\langle \delta v_0 \rangle$. We here focus on M3, the case with both Ohmic and ambipolar diffusion.

Figure 8 presents the mass loss rate (top) and energy efficiencies (bottom) against $\langle \delta v_0 \rangle$. One may find that \dot{M} drastically increases with $\langle \delta v_0 \rangle$ (red filled circles); by changing $\langle \delta v_0 \rangle$ from 1.25 km s^{-1} to 1.49 km s^{-1} , \dot{M} is enhanced by six times to reproduce the level of the current solar wind (Withbroe 1988). This sensitive dependence arises from the increasing trend of the survival fraction of the Alfvénic Poynting flux, $L_{A,tc}/L_{A,+0}$, at the transition region (open squares in the bottom panel).

To examine the radial variation of the Poynting flux, we compare L_A (blue) and L_D (red) of three non-ideal MHD cases (M3) with different $\langle \delta v_0 \rangle$ and the ideal MHD case (M0) in Figure 9. The qualitative trend of the efficient ambipolar dissipation in the chromosphere is similar in these three cases. However, a close look reveals that, although the dissipative Poynting luminosity, L_D , is larger for cases with larger $\langle \delta v_{\perp,0} \rangle$, the difference among the three cases is not as large as that of L_A . This is because the ambipolar diffusion is less efficient in denser gas (equation 21). The middle panel of Figure 10 shows that the density in the chromosphere is highest in the case with the largest $\langle \delta v_{\perp,0} \rangle$, M3-170 (green dotted line), as the gas is supported by the magnetic pressure, $B_\perp^2/8\pi$, associated with Alfvénic perturbations (blue dashed line in Figure 6), in addition to the gas pressure. As a result, the ambipolar diffusion is relatively quenched in this case, compared to that expected from the simple extrapolation from cases with smaller

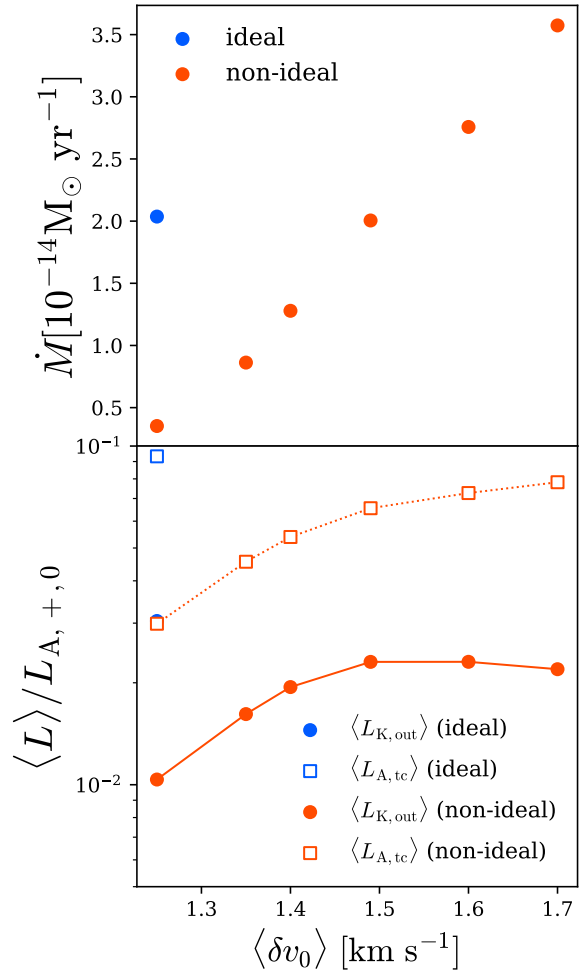


Figure 8. Dependence of \dot{M} (filled circles in top panel), $L_{A,tc}/L_{A,+0}$ (open squares in bottom panel), and $L_{K,out}/L_{A,+0}$ (filled circles in bottom panel) on $\langle \delta v_0 \rangle$. The red and blue symbols denote the results with both Ohmic and ambipolar diffusion (M3-*) and without magnetic diffusion (M0), respectively.

$\langle \delta v_{\perp,0} \rangle$. Therefore, the original case, M3, with the smallest $\langle \delta v_{\perp,0} \rangle$ suffers the severest ambipolar damping in dimensionless units, L_D/L_A , in the chromosphere. Additionally, the slower decrease of the density in the chromosphere suppresses the reflection of Alfvénic waves in cases with large $\langle \delta v_{\perp,0} \rangle$ (Suzuki & Inutsuka 2006; Suzuki et al. 2013, see also, Section 3.4). These are the reasons why the survival fraction, $L_{A,tc}/L_{A,+0}$, at the transition region increases with $\langle \delta v_{\perp,0} \rangle$ in the bottom panel of Figure 8.

The kinetic energy luminosity, $L_{K,out}/L_{A,+0}$, exhibits a similar trend to $L_{A,tc}/L_{A,+0}$, but it is slightly decreasing with $\langle \delta v_0 \rangle$ for $\langle \delta v_0 \rangle > 1.49 \text{ km s}^{-1}$. This stems from enhanced radiative cooling (Table 1), which is augmented by the increased coronal density (middle panel of Figure 10); the larger $L_{A,tc}$ heats up the corona to higher

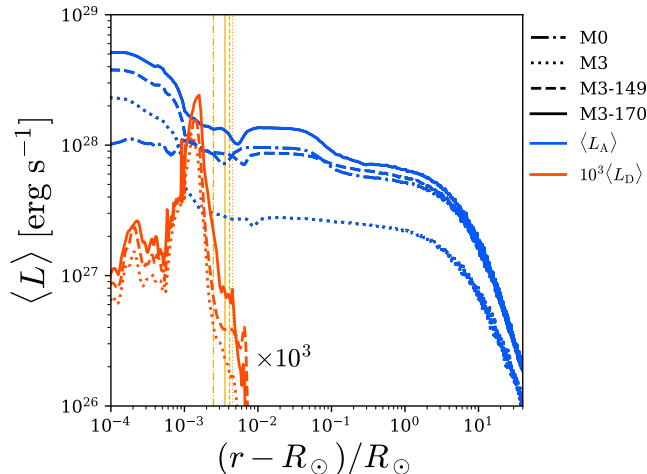


Figure 9. Time-averaged L_A (blue) and L_D (red) for M0 (dash-dotted), M3 (dotted), M3-149 (dashed), and M3-170 (solid). L_D is multiplied by 10^3 , and the vertical orange lines denote the locations at $T = 2 \times 10^4 \text{ K}$.

temperature (top panel), which promotes chromospheric evaporation. The higher coronal density yields smaller wind velocity (bottom panel of Figure 10), which is also a reason for the saturated $L_{K,\text{out}}/L_{A,+0}$. We note that both $L_{A,\text{tc}}/L_{A,+0}$ and $L_{K,\text{out}}/L_{A,+0}$ are smaller than those of the ideal MHD case with $\langle \delta v_0 \rangle = 1.25 \text{ km s}^{-1}$, M0 (blue points in Figure 8) within the range of $\langle \delta v_0 \rangle \leq 1.70 \text{ km s}^{-1}$.

In Figure 10 we are also displaying the result of the ideal MHD case (M0; blue dashed lines) to compare with that of the cases with magnetic diffusion. One can see that the diffusive case with $\langle \delta v_0 \rangle = 1.49 \text{ km s}^{-1}$ (M3-149; orange dashed lines) almost traces the ideal case with $\langle \delta v_0 \rangle = 1.25 \text{ km s}^{-1}$ in $r - R_{\odot} \gtrsim 0.5 R_{\odot}$ and gives the comparable \dot{M} (Table 1); the difference between these two cases is seen only below the low corona.

The same tendency is obtained for the amplitudes of Alfvénic waves (Figure 6). Both magnetic and velocity amplitudes of M3-149 (dashed lines) almost coincide with those of M0 (dotted lines) above $r - R_{\odot} \gtrsim R_{\odot}$. Paradoxically, $\langle b_{\perp} \rangle$ and $\langle v_{\perp} \rangle$ of M3-149 are smaller than those of M3 with smaller $\langle \delta v_0 \rangle = 1.25 \text{ km s}^{-1}$ there (solid lines) even though the Alfvénic Poynting luminosity is larger (Figure 9). This is because the density is higher by nearly an order of magnitude (middle panel of Figure 10). In other words, the higher coronal density by the boosted chromospheric evaporation can transport larger $L_A (\propto \rho v_{\perp}^2 \sim \rho b_{\perp}^2)$ to the outer region with smaller magnetic and velocity amplitudes.

4. DISCUSSIONS

4.1. Density Fluctuation

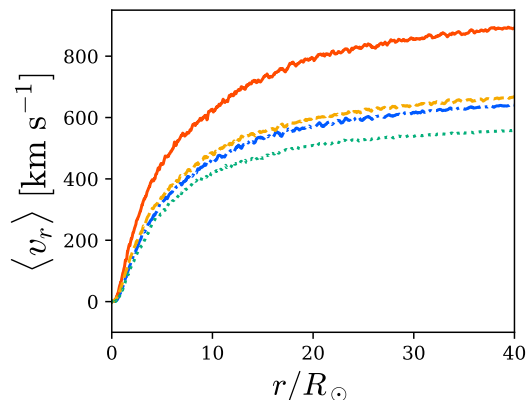
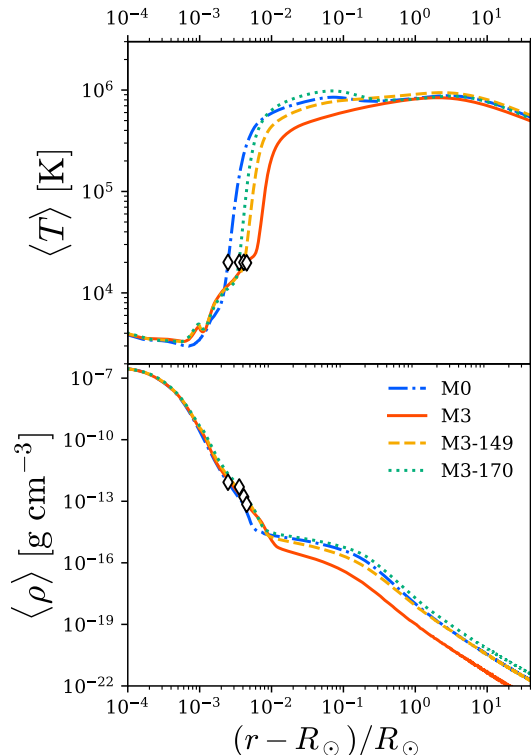


Figure 10. The same as Figure 3 but for M0 (blue dash-dotted), M3 (red solid), M3-149 (orange dashed), and M3-170 (green dotted). In the bottom panel for $\langle v_r \rangle$, the linear scale, r/R_{\odot} , is adopted for the horizontal axis.

In Section 3.5, we demonstrated that the non-ideal MHD case $\langle \delta v_0 \rangle = 1.49 \text{ km s}^{-1}$, M3-149, and the ideal MHD case with $\langle \delta v_0 \rangle = 1.25 \text{ km s}^{-1}$, M0, give similar corona and wind properties with \dot{M} being comparable to the mass loss rate of the present-day solar wind. However, as the propagation and dissipation of Alfvénic waves below the transition region are different between these two cases (Figure 9), we expect that there would be observational footprints to grab the effects of the magnetic diffusion in the low atmospheric region. As

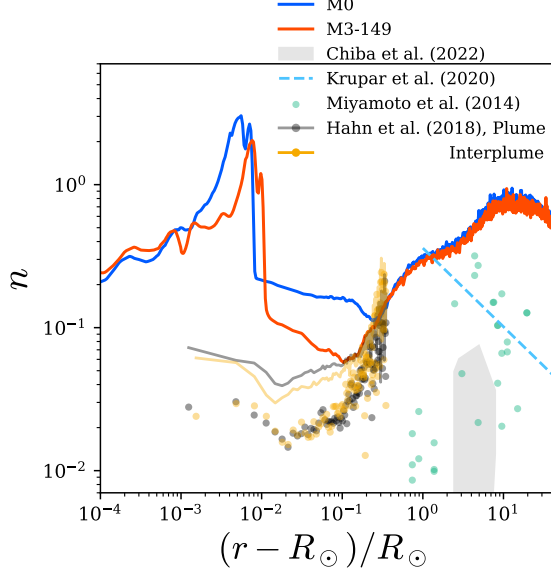


Figure 11. Time-averaged radial profile of relative density fluctuation, n , (equation 43) of M0 (blue solid line) and M3-149 (red solid line). Light blue-dashed line represents the power-law fit to observed n to explain type III radio bursts by the PSP (Krupar et al. 2020), green dots and gray area are derived from radio scintillations by Akatsuki (Imamura et al. 2014; Miyamoto et al. 2014; Chiba et al. 2022), and orange and black dots and lines are obtained from fluctuations of coronal intensity detected by PROBA2/SWAP (Hahn et al. 2018, see text for the detail).

a potential candidate for such observational signatures, we examine the radial profiles of dimensionless density fluctuation,

$$n = \frac{1}{\langle \rho \rangle} \sqrt{\langle (\rho - \langle \rho \rangle)^2 \rangle}, \quad (43)$$

normalized by the time-averaged density, $\langle \rho \rangle$, in Figure 11.

One may find a remarkable difference in n in the low coronal region, $10^{-2}R_{\odot} \lesssim r - R_{\odot} \lesssim 0.3R_{\odot}$. In our simulations, density fluctuations are excited by the variation in magnetic pressure, $B_{\perp}^2/8\pi$, with transverse waves (Hollweg 1982; Kudoh & Shibata 1999; Suzuki & Inutsuka 2005) and parametric decay instability (Goldstein 1978; Terasawa et al. 1986; Suzuki & Inutsuka 2006). In the non-ideal MHD case, higher frequency Alfvénic waves are preferentially damped by the ambipolar diffusion in the chromosphere (de Pontieu & Haerendel 1998; Leake et al. 2005; Zaqrashvili et al. 2011). As a result, only lower-frequency waves survive beyond the upper chromosphere. Hence, small-scale density fluctuations are not excited, which reduces n in the low corona. However, as small-scale structures are regenerated in the corona by the interaction between pre-existing outgoing waves and reflected waves from the upper region, n 's of

the two cases are converged in $r - R_{\odot} \gtrsim 0.3R_{\odot}$. The peak of n at $r - R_{\odot} \approx 10R_{\odot}$ is formed by the decay instability (Shoda et al. 2018b).

We also plot observed density fluctuations by various instruments in Figure 11. The numerical results exceed most of the observational data. On the one hand, MHD simulations in a 1D flux tube generally tend to overestimate density perturbations because compressible waves are confined in the tube. On the other hand, the density fluctuations estimated from radio scintillation measurements with the Akatsuki spacecraft by Miyamoto et al. (2014, green dots; see also Imamura et al. (2014)); Chiba et al. (2022, gray shade) might be underestimated if positive and negative density fluctuations were partially cancelled out along the line of sight. The similar effect may also affect the density fluctuations obtained from type III radio bursts using the Radio Frequency Spectrometer onboard the Parker Solar Probe (Krupar et al. 2020, light blue dashed line; see also Kontar et al. (2023); Krupar et al. (2024)). Observed density fluctuations in the low corona can be derived from coronal intensity variation by the Sun Watcher using the Active Pixel System detector and Image Processing on the Project for Onboard Autonomy (SWAP/PROBA2) (Hahn et al. 2018, orange and black dots and lines), where black and orange dots (lines) are obtained with a running- (average-)difference method in plume and interplume regions, respectively; the running difference approach gives more or less an "average" level of the fluctuations, while the average difference one gives an upper bound that may include spectral changes in low frequency parts. The comparison with the simulation results shows that these observational data favor the case with the non-ideal MHD effects (M3-149; red line).

4.2. 3-dimensional Magnetic Diffusion

We have ignored the Hall term and the part of ambipolar diffusion that requires the nonlinear coupling of both transverse components of magnetic field (Appendix A). Since these terms stem from drifts of particles and excite magnetic fluctuations from one component to the other, they are three dimensional processes. When the direction of wave propagation is not parallel with the magnetic field, Hall and ambipolar drifts may cause unstable phenomena; while ambipolar drifts may destabilize obliquely propagating waves, Hall instability possibly amplifies both perpendicular and oblique waves (Desch 2004; Pandey & Wardle 2012, 2013).

A typical example of the Hall instability occurs when radial shear flow generates an azimuthal magnetic field from a radial field. If the Hall drift is active, the radial magnetic field is amplified from the generated azimuthal

field; the magnetic fields of the different components are amplified each other (Pandey et al. 2008). This instability possibly occurs in the chromosphere when torsional Alfvén waves are excited by vortex motion in the photosphere (Fedun et al. 2011; Srivastava et al. 2017; Kuniyoshi et al. 2023).

Since Hall instability makes open flux tubes unstable, it may have a huge impact on our model based on the flux open flux tube, equation (1). Although the Hall term can be included in the 1D system of this study (Appendix A), this treatment is insufficient because the only small attacking angle between wave and magnetic field is allowed; the direction of wave propagation is strictly fixed along r and the direction of magnetic field is deviated from r only by B_{\perp}/B_r . The influence of Hall instability should be investigated by a multidimensional numerical model.

4.3. Low-mass Main-sequence Stars

The Alfvén-wave driven mechanism is believed to be also a promising process in driving stellar winds from low-mass main sequence stars (Cranmer & Saar 2011; Sakaue & Shibata 2021a,b; Wood et al. 2021). Compared to the Sun, the non-ideal MHD effects are probably more essential in these stars because the temperature in the photosphere is lower.

5. SUMMARY

We investigated the influence of non-ideal MHD effects on the MHD-wave-driven solar wind by performing 1D non-ideal MHD simulations with radiative cooling and thermal conduction. In the photosphere and the chromosphere the plasma is partially ionized (top panel of Figure 2) so that the non-ideal MHD effects play a significant role. The radial profile of magnetic Reynolds number (bottom panel of Figure 2) indicates that Ohmic diffusion is non-negligible from the photosphere to the low chromosphere and that ambipolar diffusion is substantially important in the chromosphere.

The magnetic-field fluctuations of Alfvénic waves from the photosphere are significantly damped by ambipolar diffusion in the chromosphere (Figures 5 and 6), reducing the Poynting flux that reaches the corona (Figure 4). As a result, the coronal temperature is lower than that obtained in the ideal MHD simulation, which suppresses the chromospheric evaporation and reduces the coronal density (Figure 3). Consequently, the mass loss rate of the model with Ohmic and ambipolar diffusion

is reduced by a factor of 6, compared with that of the ideal case (Table 1). The coronal density also decreases more rapidly with height owing to the lower coronal temperature, and hence, a larger fraction of the outgoing Alfvénic waves is reflected to give higher Elsässer ratio in the corona because of the larger gradient of the Alfvén velocity (Figure 7).

We also found that the physical properties of the corona and wind sensitively depends on the amplitude of velocity fluctuations, $\langle \delta v_0 \rangle$, at the photosphere. When $\langle \delta v_0 \rangle$ is increased from our standard value, 1.25 km s^{-1} to 1.49 km s^{-1} , which corresponds to the increase of the input energy ($\propto \langle \delta v_0^2 \rangle$) by $\approx 40\%$, the mass loss rate is enhanced to six times the original value to recover the mass loss rate obtained in the present-day solar wind (top panel of Figure 8). This is firstly because ambipolar dissipation is quenched in the higher-density chromosphere (Figure 9) and secondly because the reflection of Alfvénic waves is suppressed. As a consequence, a larger fraction of the Alfvénic Poynting flux injected from the photosphere is transported to the corona (bottom of Figure 8 and Table 1), resulting in hotter corona and denser wind (Figure 10).

The non-ideal MHD case with $\langle \delta v_0 \rangle = 1.49 \text{ km s}^{-1}$ and the ideal MHD case with $\langle \delta v_0 \rangle = 1.25 \text{ km s}^{-1}$ give similar structures of the corona and solar wind. However, the density fluctuation of the non-ideal MHD case is smaller in the low coronal region because ambipolar diffusion selectively damps high-frequency Alfvénic waves to quench the excitation of short-wavelength compressible perturbations by the parametric decay instability and the nonlinear mode conversion. Density perturbations in the corona can be used as an observational signature of the non-ideal MHD dissipation of MHD waves in the chromosphere.

ACKNOWLEDGMENTS

We thank M. Hahn, T. Imamura, and V. Krupar for providing observational data and valuable comments. Numerical computations were in part carried out on PC cluster at Center for Computational Astrophysics, National Astronomical Observatory of Japan. T.K.S. is supported by Grants-in-Aid for Scientific Research from the MEXT/JSPS of Japan, 22H01263. T.T. is supported by IGPEES, WINGS Program in the University of Tokyo and Research Fellowships for Young Scientists, JSPS.

APPENDIX

A. HALL AND AMBIPOLAR DIFFUSION TERMS

The Hall and ambipolar diffusion terms in the induction equation (7) are written as

$$\begin{aligned} \frac{\partial \mathbf{B}}{\partial t} = & \dots + \nabla \times [-\eta_{\text{H}}(\nabla \times \mathbf{B}) \times \hat{\mathbf{e}}_B] \\ & + \eta_{\text{AD}}((\nabla \times \mathbf{B}) \times \hat{\mathbf{e}}_B) \times \hat{\mathbf{e}}_B, \end{aligned} \quad (\text{A1})$$

where $\eta_H \equiv \frac{c|B|}{4\pi n_e e c}$ is the Hall diffusivity and \hat{e}_B is the unit vector along a magnetic field line. In our 1D simulations with the coordinate system, equation (8), the Hall part is explicitly expressed as

$$\left. \frac{\partial B_{\perp 1(2)}}{\partial t} \right|_H = \pm \frac{1}{r\sqrt{f}} \frac{\partial}{\partial r} \left[\eta_H \frac{\partial}{\partial r} (B_{\perp 2(1)} r \sqrt{f}) B_r \right], \quad (\text{A2})$$

which generates the first (second) transverse component from the second (first) component. We ignore this term although in a strictly speaking even our "1 $\frac{2}{2}$ " coordinate system can consider it.

For the ambipolar diffusion part, we have

$$\left. \frac{\partial B_{\perp 1(2)}}{\partial t} \right|_{AD} = \frac{1}{r\sqrt{f}} \frac{\partial}{\partial r} \left[\eta_{AD} \frac{\partial}{\partial r} (B_{\perp 1(2)} r \sqrt{f}) \right] + \frac{\eta_{AD}}{B^2} \left\{ \frac{\partial}{\partial r} (B_{\perp 2(1)} r \sqrt{f}) B_{\perp 1} B_{\perp 2} - \frac{\partial}{\partial r} (B_{\perp 1(2)} r \sqrt{f}) B_{\perp 2(1)}^2 \right\}. \quad (\text{A3})$$

We only considered the first term on the right-hand side, which corresponds to isotropic diffusion. We ignore the other terms, which require nonlinear coupling between the two transverse components.

REFERENCES

- Abramenko, V. I., Yurchyshyn, V. B., Goode, P. R., Kitiashvili, I. N., & Kosovichev, A. G. 2012, *ApJL*, 756, L27, doi: [10.1088/2041-8205/756/2/L27](https://doi.org/10.1088/2041-8205/756/2/L27)
- Alazraki, G., & Couturier, P. 1971, *A&A*, 13, 380
- Alfvén, H. 1947, *MNRAS*, 107, 211, doi: [10.1093/mnras/107.2.211](https://doi.org/10.1093/mnras/107.2.211)
- An, C. H., Suess, S. T., Moore, R. L., & Musielak, Z. E. 1990, *ApJ*, 350, 309, doi: [10.1086/168384](https://doi.org/10.1086/168384)
- Anderson, L. S., & Athay, R. G. 1989, *ApJ*, 336, 1089, doi: [10.1086/167078](https://doi.org/10.1086/167078)
- Anfinogentov, S. A., Nakariakov, V. M., & Nisticò, G. 2015, *A&A*, 583, A136, doi: [10.1051/0004-6361/201526195](https://doi.org/10.1051/0004-6361/201526195)
- Antolin, P., Okamoto, T. J., De Pontieu, B., et al. 2015, *ApJ*, 809, 72, doi: [10.1088/0004-637X/809/1/72](https://doi.org/10.1088/0004-637X/809/1/72)
- Arber, T. D., Brady, C. S., & Shelyag, S. 2016, *ApJ*, 817, 94, doi: [10.3847/0004-637X/817/2/94](https://doi.org/10.3847/0004-637X/817/2/94)
- Asplund, M., Grevesse, N., Sauval, A. J., & Scott, P. 2009, *ARA&A*, 47, 481, doi: [10.1146/annurev.astro.46.060407.145222](https://doi.org/10.1146/annurev.astro.46.060407.145222)
- Banerjee, D., Krishna Prasad, S., Pant, V., et al. 2021, *SSRv*, 217, 76, doi: [10.1007/s11214-021-00849-0](https://doi.org/10.1007/s11214-021-00849-0)
- Belcher, J. W. 1971, *ApJ*, 168, 509, doi: [10.1086/151105](https://doi.org/10.1086/151105)
- Berger, T. E., Löfdahl, M. G., Shine, R. S., & Title, A. M. 1998, *ApJ*, 495, 973, doi: [10.1086/305309](https://doi.org/10.1086/305309)
- Berger, T. E., & Title, A. M. 2001, *ApJ*, 553, 449, doi: [10.1086/320663](https://doi.org/10.1086/320663)
- Blaes, O. M., & Balbus, S. A. 1994, *ApJ*, 421, 163, doi: [10.1086/173634](https://doi.org/10.1086/173634)
- Braginskii, S. I. 1965, *Reviews of Plasma Physics*, 1, 205
- Brandenburg, A., & Zweibel, E. G. 1994, *ApJL*, 427, L91, doi: [10.1086/187372](https://doi.org/10.1086/187372)
- Castelli, F., & Kurucz, R. L. 2003, in *Modelling of Stellar Atmospheres*, ed. N. Piskunov, W. W. Weiss, & D. F. Gray, Vol. 210, A20, doi: [10.48550/arXiv.astro-ph/0405087](https://doi.org/10.48550/arXiv.astro-ph/0405087)
- Chiba, S., Imamura, T., Tokumaru, M., et al. 2022, in *AGU Fall Meeting Abstracts*, Vol. 2022, P41D-01
- Chitta, L. P., van Ballegooijen, A. A., Rouppe van der Voort, L., DeLuca, E. E., & Kariyappa, R. 2012, *ApJ*, 752, 48, doi: [10.1088/0004-637X/752/1/48](https://doi.org/10.1088/0004-637X/752/1/48)
- Cranmer, S. R., & Saar, S. H. 2011, *ApJ*, 741, 54, doi: [10.1088/0004-637X/741/1/54](https://doi.org/10.1088/0004-637X/741/1/54)
- Cranmer, S. R., van Ballegooijen, A. A., & Edgar, R. J. 2007, *ApJS*, 171, 520, doi: [10.1086/518001](https://doi.org/10.1086/518001)
- de Pontieu, B., & Haerendel, G. 1998, *A&A*, 338, 729
- Desch, S. J. 2004, *ApJ*, 608, 509, doi: [10.1086/392527](https://doi.org/10.1086/392527)
- Draine, B. T., Roberge, W. G., & Dalgarno, A. 1983, *ApJ*, 264, 485, doi: [10.1086/160617](https://doi.org/10.1086/160617)
- Elsasser, W. M. 1950, *Physical Review*, 79, 183, doi: [10.1103/PhysRev.79.183](https://doi.org/10.1103/PhysRev.79.183)
- Fedun, V., Shelyag, S., Verth, G., Mathioudakis, M., & Erdélyi, R. 2011, *Annales Geophysicae*, 29, 1029, doi: [10.5194/angeo-29-1029-2011](https://doi.org/10.5194/angeo-29-1029-2011)
- Gary, G. A. 2001, *SoPh*, 203, 71, doi: [10.1023/A:1012722021820](https://doi.org/10.1023/A:1012722021820)
- Goldstein, M. L. 1978, *ApJ*, 219, 700, doi: [10.1086/155829](https://doi.org/10.1086/155829)
- Grappin, R., Aulanier, G., & Pinto, R. 2008, *A&A*, 490, 353, doi: [10.1051/0004-6361:200810386](https://doi.org/10.1051/0004-6361:200810386)
- Hahn, M., D’Huys, E., & Savin, D. W. 2018, *ApJ*, 860, 34, doi: [10.3847/1538-4357/aac0f3](https://doi.org/10.3847/1538-4357/aac0f3)
- Hahn, M., & Savin, D. W. 2013, *ApJ*, 776, 78, doi: [10.1088/0004-637X/776/2/78](https://doi.org/10.1088/0004-637X/776/2/78)
- Hara, H. 2019, *ApJ*, 887, 122, doi: [10.3847/1538-4357/ab50bf](https://doi.org/10.3847/1538-4357/ab50bf)
- Harper, G. M., Richter, M. J., Ryde, N., et al. 2009, *ApJ*, 701, 1464, doi: [10.1088/0004-637X/701/2/1464](https://doi.org/10.1088/0004-637X/701/2/1464)
- Hartmann, L., & Avrett, E. H. 1984, *ApJ*, 284, 238, doi: [10.1086/162402](https://doi.org/10.1086/162402)
- Heyvaerts, J., & Priest, E. R. 1983, *A&A*, 117, 220
- Hollweg, J. V. 1982, *ApJ*, 254, 806, doi: [10.1086/159791](https://doi.org/10.1086/159791)
- . 1984, *SoPh*, 91, 269, doi: [10.1007/BF00146299](https://doi.org/10.1007/BF00146299)

- . 1986, *J. Geophys. Res.*, 91, 4111, doi: [10.1029/JA091iA04p04111](https://doi.org/10.1029/JA091iA04p04111)
- Hossain, M., Gray, P. C., Pontius, Duane H., J., Matthaeus, W. H., & Oughton, S. 1995, *Physics of Fluids*, 7, 2886, doi: [10.1063/1.868665](https://doi.org/10.1063/1.868665)
- Imamura, T., Tokumaru, M., Isobe, H., et al. 2014, *ApJ*, 788, 117, doi: [10.1088/0004-637X/788/2/117](https://doi.org/10.1088/0004-637X/788/2/117)
- Ionson, J. A. 1978, *ApJ*, 226, 650, doi: [10.1086/156648](https://doi.org/10.1086/156648)
- Jess, D. B., Jafarzadeh, S., Keys, P. H., et al. 2023, *Living Reviews in Solar Physics*, 20, 1, doi: [10.1007/s41116-022-00035-6](https://doi.org/10.1007/s41116-022-00035-6)
- Khodachenko, M. L., Arber, T. D., Rucker, H. O., & Hanslmeier, A. 2004, *A&A*, 422, 1073, doi: [10.1051/0004-6361:20034207](https://doi.org/10.1051/0004-6361:20034207)
- Khomenko, E., & Collados, M. 2012, *ApJ*, 747, 87, doi: [10.1088/0004-637X/747/2/87](https://doi.org/10.1088/0004-637X/747/2/87)
- Khomenko, E., Collados, M., Díaz, A., & Vitas, N. 2014, *Physics of Plasmas*, 21, 092901, doi: [10.1063/1.4894106](https://doi.org/10.1063/1.4894106)
- Kontar, E. P., Emslie, A. G., Clarkson, D. L., et al. 2023, *ApJ*, 956, 112, doi: [10.3847/1538-4357/acf6c1](https://doi.org/10.3847/1538-4357/acf6c1)
- Kopp, R. A., & Holzer, T. E. 1976, *SoPh*, 49, 43, doi: [10.1007/BF00221484](https://doi.org/10.1007/BF00221484)
- Koyama, H., & Inutsuka, S.-I. 2000, *ApJ*, 532, 980, doi: [10.1086/308594](https://doi.org/10.1086/308594)
- Krupar, V., Kruparova, O., Szabo, A., et al. 2024, *ApJ*, 960, 101, doi: [10.3847/1538-4357/ad150e](https://doi.org/10.3847/1538-4357/ad150e)
- Krupar, V., Szabo, A., Maksimovic, M., et al. 2020, *ApJS*, 246, 57, doi: [10.3847/1538-4365/ab65bd](https://doi.org/10.3847/1538-4365/ab65bd)
- Kudoh, T., & Shibata, K. 1999, *ApJ*, 514, 493, doi: [10.1086/306930](https://doi.org/10.1086/306930)
- Kuniyoshi, H., Shoda, M., Iijima, H., & Yokoyama, T. 2023, *ApJ*, 949, 8, doi: [10.3847/1538-4357/accbb8](https://doi.org/10.3847/1538-4357/accbb8)
- Kurucz, R. L. 1979, *ApJS*, 40, 1, doi: [10.1086/190589](https://doi.org/10.1086/190589)
- Leake, J. E., Arber, T. D., & Khodachenko, M. L. 2005, *A&A*, 442, 1091, doi: [10.1051/0004-6361:20053427](https://doi.org/10.1051/0004-6361:20053427)
- Martínez-Sykora, J., de la Cruz Rodríguez, J., Gošić, M., et al. 2023, *ApJL*, 943, L14, doi: [10.3847/2041-8213/acafe9](https://doi.org/10.3847/2041-8213/acafe9)
- Martínez-Sykora, J., De Pontieu, B., & Hansteen, V. 2012, *ApJ*, 753, 161, doi: [10.1088/0004-637X/753/2/161](https://doi.org/10.1088/0004-637X/753/2/161)
- Mathis, J. S., Mezger, P. G., & Panagia, N. 1983, *A&A*, 128, 212
- Matsumoto, T. 2018, *MNRAS*, 476, 3328, doi: [10.1093/mnras/sty490](https://doi.org/10.1093/mnras/sty490)
- Matsumoto, T., & Kitai, R. 2010, *ApJL*, 716, L19, doi: [10.1088/2041-8205/716/1/L19](https://doi.org/10.1088/2041-8205/716/1/L19)
- Matsumoto, T., & Suzuki, T. K. 2012, *ApJ*, 749, 8, doi: [10.1088/0004-637X/749/1/8](https://doi.org/10.1088/0004-637X/749/1/8)
- . 2014, *MNRAS*, 440, 971, doi: [10.1093/mnras/stu310](https://doi.org/10.1093/mnras/stu310)
- Matthaeus, W. H., Zank, G. P., Smith, C. W., & Oughton, S. 1999, *PhRvL*, 82, 3444, doi: [10.1103/PhysRevLett.82.3444](https://doi.org/10.1103/PhysRevLett.82.3444)
- McIntosh, S. W., de Pontieu, B., Carlsson, M., et al. 2011, *Nature*, 475, 477, doi: [10.1038/nature10235](https://doi.org/10.1038/nature10235)
- McMurdo, M., Ballai, I., Verth, G., Alharbi, A., & Fedun, V. 2023, *ApJ*, 958, 81, doi: [10.3847/1538-4357/ad0364](https://doi.org/10.3847/1538-4357/ad0364)
- Mestel, L., & Spitzer, L., J. 1956, *MNRAS*, 116, 503, doi: [10.1093/mnras/116.5.503](https://doi.org/10.1093/mnras/116.5.503)
- Miyamoto, M., Imamura, T., Tokumaru, M., et al. 2014, *ApJ*, 797, 51, doi: [10.1088/0004-637X/797/1/51](https://doi.org/10.1088/0004-637X/797/1/51)
- Moore, R. L., Musielak, Z. E., Suess, S. T., & An, C. H. 1991, *ApJ*, 378, 347, doi: [10.1086/170435](https://doi.org/10.1086/170435)
- Morton, R. J., Sharma, R., Tajfrouze, E., & Miriyala, H. 2023, *Reviews of Modern Plasma Physics*, 7, 17, doi: [10.1007/s41614-023-00118-3](https://doi.org/10.1007/s41614-023-00118-3)
- Nakariakov, V. M., Ofman, L., Deluca, E. E., Roberts, B., & Davila, J. M. 1999, *Science*, 285, 862, doi: [10.1126/science.285.5429.862](https://doi.org/10.1126/science.285.5429.862)
- November, L. J., & Simon, G. W. 1988, *ApJ*, 333, 427, doi: [10.1086/166758](https://doi.org/10.1086/166758)
- Oba, T., Iida, Y., & Shimizu, T. 2017, *ApJ*, 836, 40, doi: [10.3847/1538-4357/836/1/40](https://doi.org/10.3847/1538-4357/836/1/40)
- . 2020, *ApJ*, 890, 141, doi: [10.3847/1538-4357/ab6a90](https://doi.org/10.3847/1538-4357/ab6a90)
- Ofman, L., & Davila, J. M. 1995, *J. Geophys. Res.*, 100, 23427, doi: [10.1029/95JA01907](https://doi.org/10.1029/95JA01907)
- Okamoto, T. J., Antolin, P., De Pontieu, B., et al. 2015, *ApJ*, 809, 71, doi: [10.1088/0004-637X/809/1/71](https://doi.org/10.1088/0004-637X/809/1/71)
- Okamoto, T. J., & De Pontieu, B. 2011, *ApJL*, 736, L24, doi: [10.1088/2041-8205/736/2/L24](https://doi.org/10.1088/2041-8205/736/2/L24)
- Osterbrock, D. E. 1961, *ApJ*, 134, 347, doi: [10.1086/147165](https://doi.org/10.1086/147165)
- Pandey, B. P., Vranjes, J., & Krishan, V. 2008, *MNRAS*, 386, 1635, doi: [10.1111/j.1365-2966.2008.13144.x](https://doi.org/10.1111/j.1365-2966.2008.13144.x)
- Pandey, B. P., & Wardle, M. 2012, *MNRAS*, 426, 1436, doi: [10.1111/j.1365-2966.2012.21718.x](https://doi.org/10.1111/j.1365-2966.2012.21718.x)
- . 2013, *MNRAS*, 431, 570, doi: [10.1093/mnras/stt184](https://doi.org/10.1093/mnras/stt184)
- Parker, E. N. 1953, *ApJ*, 117, 431, doi: [10.1086/145707](https://doi.org/10.1086/145707)
- Piddington, J. H. 1956, *MNRAS*, 116, 314, doi: [10.1093/mnras/116.3.314](https://doi.org/10.1093/mnras/116.3.314)
- Popescu Braileanu, B., & Keppens, R. 2021, *A&A*, 653, A131, doi: [10.1051/0004-6361/202140872](https://doi.org/10.1051/0004-6361/202140872)
- Réville, V., Tenerani, A., & Velli, M. 2018, *ApJ*, 866, 38, doi: [10.3847/1538-4357/aadb8f](https://doi.org/10.3847/1538-4357/aadb8f)
- Rosner, R., Tucker, W. H., & Vaiana, G. S. 1978, *ApJ*, 220, 643, doi: [10.1086/155949](https://doi.org/10.1086/155949)
- Roudier, T., & Muller, R. 1986, *SoPh*, 107, 11, doi: [10.1007/BF00155337](https://doi.org/10.1007/BF00155337)
- Sakaue, T., & Shibata, K. 2020, *ApJ*, 900, 120, doi: [10.3847/1538-4357/ababa0](https://doi.org/10.3847/1538-4357/ababa0)
- . 2021a, *ApJL*, 906, L13, doi: [10.3847/2041-8213/abd3a9](https://doi.org/10.3847/2041-8213/abd3a9)

- . 2021b, *ApJ*, 919, 29, doi: [10.3847/1538-4357/ac0e34](https://doi.org/10.3847/1538-4357/ac0e34)
- Sakurai, T., & Granik, A. 1984, *ApJ*, 277, 404, doi: [10.1086/161707](https://doi.org/10.1086/161707)
- Schmidt, M. 1966, *ApJ*, 146, 7, doi: [10.1086/148854](https://doi.org/10.1086/148854)
- Sharma, R., & Morton, R. J. 2023, *Nature Astronomy*, 7, 1301, doi: [10.1038/s41550-023-02070-1](https://doi.org/10.1038/s41550-023-02070-1)
- Shelyag, S., Khomenko, E., de Vicente, A., & Przybylski, D. 2016, *ApJL*, 819, L11, doi: [10.3847/2041-8205/819/1/L11](https://doi.org/10.3847/2041-8205/819/1/L11)
- Shimizu, K., Shoda, M., & Suzuki, T. K. 2022, *ApJ*, 931, 37, doi: [10.3847/1538-4357/ac66d7](https://doi.org/10.3847/1538-4357/ac66d7)
- Shoda, M., Suzuki, T. K., Asgari-Targhi, M., & Yokoyama, T. 2019, *ApJL*, 880, L2, doi: [10.3847/2041-8213/ab2b45](https://doi.org/10.3847/2041-8213/ab2b45)
- Shoda, M., & Yokoyama, T. 2016, *ApJ*, 820, 123, doi: [10.3847/0004-637X/820/2/123](https://doi.org/10.3847/0004-637X/820/2/123)
- Shoda, M., Yokoyama, T., & Suzuki, T. K. 2018a, *ApJ*, 853, 190, doi: [10.3847/1538-4357/aaa3e1](https://doi.org/10.3847/1538-4357/aaa3e1)
- . 2018b, *ApJ*, 860, 17, doi: [10.3847/1538-4357/aac218](https://doi.org/10.3847/1538-4357/aac218)
- Soler, R., Carbonell, M., & Ballester, J. L. 2015, *ApJ*, 810, 146, doi: [10.1088/0004-637X/810/2/146](https://doi.org/10.1088/0004-637X/810/2/146)
- Soler, R., Díaz, A. J., Ballester, J. L., & Goossens, M. 2013, *A&A*, 551, A86, doi: [10.1051/0004-6361/201220576](https://doi.org/10.1051/0004-6361/201220576)
- Spitzer, L. 1962, *Physics of Fully Ionized Gases*
- Srivastava, A. K., Shetye, J., Murawski, K., et al. 2017, *Scientific Reports*, 7, 43147, doi: [10.1038/srep43147](https://doi.org/10.1038/srep43147)
- Sutherland, R. S., & Dopita, M. A. 1993, *ApJS*, 88, 253, doi: [10.1086/191823](https://doi.org/10.1086/191823)
- Suzuki, T. K. 2002, *ApJ*, 578, 598, doi: [10.1086/342347](https://doi.org/10.1086/342347)
- . 2004, *MNRAS*, 349, 1227, doi: [10.1111/j.1365-2966.2004.07570.x](https://doi.org/10.1111/j.1365-2966.2004.07570.x)
- . 2018, *PASJ*, 70, 34, doi: [10.1093/pasj/psy023](https://doi.org/10.1093/pasj/psy023)
- Suzuki, T. K., Imada, S., Kataoka, R., et al. 2013, *PASJ*, 65, 98, doi: [10.1093/pasj/65.5.98](https://doi.org/10.1093/pasj/65.5.98)
- Suzuki, T. K., & Inutsuka, S.-i. 2005, *ApJL*, 632, L49, doi: [10.1086/497536](https://doi.org/10.1086/497536)
- Suzuki, T. K., & Inutsuka, S.-I. 2006, *Journal of Geophysical Research (Space Physics)*, 111, A06101, doi: [10.1029/2005JA011502](https://doi.org/10.1029/2005JA011502)
- Tenerani, A., Velli, M., & Hellinger, P. 2017, *ApJ*, 851, 99, doi: [10.3847/1538-4357/aa9bef](https://doi.org/10.3847/1538-4357/aa9bef)
- Terasawa, T., Hoshino, M., Sakai, J. I., & Hada, T. 1986, *J. Geophys. Res.*, 91, 4171, doi: [10.1029/JA091iA04p04171](https://doi.org/10.1029/JA091iA04p04171)
- Title, A. M., Tarbell, T. D., Topka, K. P., et al. 1989, *ApJ*, 336, 475, doi: [10.1086/167026](https://doi.org/10.1086/167026)
- Tomczyk, S., McIntosh, S. W., Keil, S. L., et al. 2007, *Science*, 317, 1192, doi: [10.1126/science.1143304](https://doi.org/10.1126/science.1143304)
- Uchida, Y., & Kaburaki, O. 1974, *SoPh*, 35, 451, doi: [10.1007/BF00151968](https://doi.org/10.1007/BF00151968)
- van Ballegooijen, A. A., & Asgari-Targhi, M. 2017, *ApJ*, 835, 10, doi: [10.3847/1538-4357/835/1/10](https://doi.org/10.3847/1538-4357/835/1/10)
- Van Doorselaere, T., Srivastava, A. K., Antolin, P., et al. 2020, *SSRv*, 216, 140, doi: [10.1007/s11214-020-00770-y](https://doi.org/10.1007/s11214-020-00770-y)
- Verdini, A., Grappin, R., & Velli, M. 2012, *A&A*, 538, A70, doi: [10.1051/0004-6361/201118046](https://doi.org/10.1051/0004-6361/201118046)
- Verdini, A., & Velli, M. 2007, *ApJ*, 662, 669, doi: [10.1086/510710](https://doi.org/10.1086/510710)
- Vernazza, J. E., Avrett, E. H., & Loeser, R. 1981, *ApJS*, 45, 635, doi: [10.1086/190731](https://doi.org/10.1086/190731)
- Washinoue, H., Shoda, M., & Suzuki, T. K. 2022, *ApJ*, 938, 126, doi: [10.3847/1538-4357/ac91c8](https://doi.org/10.3847/1538-4357/ac91c8)
- Washinoue, H., & Suzuki, T. K. 2023, *ApJ*, 953, 74, doi: [10.3847/1538-4357/ace106](https://doi.org/10.3847/1538-4357/ace106)
- Wiegelmann, T., Thalmann, J. K., & Solanki, S. K. 2014, *A&A Rv*, 22, 78, doi: [10.1007/s00159-014-0078-7](https://doi.org/10.1007/s00159-014-0078-7)
- Withbroe, G. L. 1988, *ApJ*, 325, 442, doi: [10.1086/166015](https://doi.org/10.1086/166015)
- Wood, B. E., Müller, H. R., Zank, G. P., Linsky, J. L., & Redfield, S. 2005, *ApJL*, 628, L143, doi: [10.1086/432716](https://doi.org/10.1086/432716)
- Wood, B. E., Müller, H.-R., Redfield, S., et al. 2021, *ApJ*, 915, 37, doi: [10.3847/1538-4357/abfda5](https://doi.org/10.3847/1538-4357/abfda5)
- Yasuda, Y., Suzuki, T. K., & Kozasa, T. 2019, *ApJ*, 879, 77, doi: [10.3847/1538-4357/ab23f7](https://doi.org/10.3847/1538-4357/ab23f7)
- Yuan, D., Fu, L., Cao, W., et al. 2023, *Nature Astronomy*, 7, 856, doi: [10.1038/s41550-023-01973-3](https://doi.org/10.1038/s41550-023-01973-3)
- Zaqarashvili, T. V., Khodachenko, M. L., & Rucker, H. O. 2011, *A&A*, 534, A93, doi: [10.1051/0004-6361/201117380](https://doi.org/10.1051/0004-6361/201117380)
- Zweibel, E. G. 2015, in *Astrophysics and Space Science Library*, Vol. 407, *Magnetic Fields in Diffuse Media*, ed. A. Lazarian, E. M. de Gouveia Dal Pino, & C. Melioli, 285, doi: [10.1007/978-3-662-44625-6_11](https://doi.org/10.1007/978-3-662-44625-6_11)